

Basement membrane sliding and targeted adhesion remodels tissue boundaries during uterine–vulval attachment in *Caenorhabditis elegans*

Shinji Ihara¹, Elliott J. Hagedorn¹, Meghan A. Morrissey¹, Qiuyi Chi¹, Fumio Motegi², James M. Kramer³ and David R. Sherwood^{1,4}

Large gaps in basement membrane occur at sites of cell invasion and tissue remodelling in development and cancer. Though never followed directly *in vivo*, basement membrane dissolution or reduced synthesis have been postulated to create these gaps. Using landmark photobleaching and optical highlighting of laminin and type IV collagen, we find that a new mechanism, basement membrane sliding, underlies basement membrane gap enlargement during uterine–vulval attachment in *Caenorhabditis elegans*. Laser ablation and mutant analysis reveal that the invaginating vulval cells promote basement membrane movement. Further, an RNA interference and expression screen identifies the integrin INA-1/PAT-3 and VAB-19, homologue of the tumour suppressor Kank, as regulators of basement membrane opening. Both concentrate within vulval cells at the basement membrane gap boundary and halt expansion of the shifting basement membrane. Basement membrane sliding followed by targeted adhesion represents a new mechanism for creating precise basement membrane breaches that can be used by cells to break down compartment boundaries.

Cells navigate complex networks of extracellular matrix during many developmental, physiological and pathogenic processes^{1,2}. One of the main matrix barriers that cells encounter is basement membrane, a thin, dense, sheet-like structure built on a network of polymeric laminin and type IV collagen. Basement membranes are ubiquitous in multicellular animals, enveloping most tissues and providing the structural underpinning for all epithelia and endothelia³. Cell–basement membrane interactions have been difficult to experimentally examine *in vivo* and problematic to recapitulate *in vitro*, owing to the complexities of native basement membrane structure and cellular environment^{4–6}. Thus, the mechanisms that cells use to remodel basement membrane barriers remain poorly understood.

De novo gaps in basement membrane form during developmental processes such as gastrulation and organogenesis, and facilitate tissue remodelling and cell movement^{7–9}. Metastatic tumours are thought to use the same molecular programmes to create gaps to enable their spread^{5,10–14}. The expression of matrix-degrading proteases and the presence of type IV collagen degradation products surrounding and within invasive cells has led to the idea that basement membrane barriers are overcome through proteolytic degradation^{15–22}. Based in part on these observations, inhibitors of matrix metalloproteinases have been used in clinical trials for patients with advanced cancer, though

patient survival was not increased¹⁸. Reduced basement membrane synthesis and changes in composition have also been postulated to underlie localized loss^{11,14,23}. To resolve the mechanisms that cells use to overcome basement membrane barriers it is crucial to follow the fate of breached basement membrane *in vivo* and experimentally examine the removal mechanisms.

Anchor cell invasion into the vulval epithelium in *Caenorhabditis elegans* is an experimentally and visually accessible model of invasion through basement membrane⁸. The anchor cell is a specialized gonadal cell that breaches the juxtaposed gonadal and ventral epidermal basement membranes, and contacts the central 1°-fated vulval precursor cells to initiate uterine–vulval attachment. After anchor cell invasion, neighbouring uterine and vulval cells attach to complete uterine–vulval connection²⁴. The fate of the basement membrane during these later phases of attachment is unknown.

Using cell- and basement-membrane-specific markers we report here that the breach in the basement membrane widens markedly during the later stages of uterine–vulval attachment. Landmark photobleaching and optical marking of laminin and type IV collagen reveal that neither reduced basement membrane deposition nor dissolution account for basement membrane gap expansion. Instead, we show that the basement membrane breach is widened through basement membrane

¹Department of Biology, Duke University, Science Drive, Box 90388, Durham, North Carolina 27708, USA. ²Department of Molecular Biology and Genetics, Howard Hughes Medical Institute, Center for Cell Dynamics, Johns Hopkins School of Medicine, Baltimore, Maryland 21205, USA. ³Department of Cell and Molecular Biology, Northwestern University Medical School, Chicago, Illinois 60611, USA.

⁴Correspondence should be addressed to D.R.S. (e-mail: david.sherwood@duke.edu)

sliding, and that this shift is dependent on the invaginating vulval cells. Further, we find that the integrin heterodimer INA-1/PAT-3, and VAB-19, the *C. elegans* homologue of the tumour suppressor protein Kank^{25,26}, localize within the vulval cells at the basement membrane gap boundary and halt basement membrane sliding. These studies reveal a new mechanism to widen and stabilize basement membrane breaches during tissue remodelling.

RESULTS

Summary of uterine–vulval attachment

During the mid-L3 larval stage, the ventral uterine and vulval-precursor cells (VPCs, P5.p–P7.p cell daughters) are separated by the juxtaposed gonadal and ventral-epidermal basement membranes (Fig. 1a). During the mid-to-late L3 larval stage, a specialized uterine cell, the anchor cell, initiates uterine–vulval attachment by invading through both basement membranes and contacting the underlying descendants of the 1°-fated daughters of the VPC P6.p (P6.p four-cell stage; ref. 8). Following invasion, the underlying vulval cells divide and invaginate. By the early L4 stage, the anchor cell fuses with neighbouring ventral uterine cells and forms the multinucleated utse cell, which together with the ventral uterine uv1 cells contact the 1°-fated great-granddaughters of P6.p, completing the direct connection between the uterine and vulval tissues^{24,27,28}. The vulD cells (innermost granddaughters of the 2°-fated VPCs, P5.p and P7.p) and the uv2, uv3 (descendants of dorsal uterine cells) and ut cells (descendants of ventral uterine cells) sit adjacent to the connection on the vulval and uterine sides, respectively (Fig. 1a). During these later stages of uterine–vulval attachment, the fate and dynamics of the basement membrane is unknown.

The breach in the basement membrane expands and stabilizes over the vulD cells

To examine basement membrane localization during uterine–vulval attachment we used a functional translational fusion of the lone laminin β -subunit to green fluorescent protein (laminin::GFP), which shows identical expression to immunolocalized laminin^{8,29}. The anchor cell plasma membrane was viewed using the pleckstrin-homology (PH) domain from phospholipase C- δ fused to mCherry (mCherry::PLC δ^{PH} ; ref. 30) and driven by an anchor-cell-specific promoter *cdh-3*. During the time of anchor cell invasion (P6.p four-cell stage), the anchor cell remained in direct contact with the basement membrane breach, which was positioned over the central P6.p granddaughters (Fig. 1b,c and Supplementary Movies S1 and S2). Separation of the uterine and vulval tissues' tightly juxtaposed basement membranes revealed that they became fused at the borders of the invading anchor cell and formed a continuous basement membrane throughout uterine–vulval attachment (Fig. 1g). When the vulval cells initiated invagination, the initial breach in the basement membrane widened to extend over the outer P6.p granddaughters and expanded beyond the anchor cell plasma membrane (Fig. 1d,h and Supplementary Movie S3). This expansion continued during the early P6.p eight-cell stage and then stabilized over the vulD cells (Fig. 1e and Supplementary Movie S4), a position directly abutting the multinucleate uterine utse cell in the mid-L4 stage (Fig. 1f, h). Transgenic animals expressing the basement membrane components SPARC, secreted protein acidic and rich in cysteine (*sparc::GFP*), and the sole *C. elegans* α 1-like type IV collagen chain (*type IV*

collagen::mCherry; refs 31,32), showed identical basement membrane gap positioning. Thus, the breach in the basement membrane widens beyond the anchor cell and stabilizes over the vulD cells at the L4 stage during uterine–vulval attachment.

The anchor cell initiates but does not complete basement membrane gap formation

To determine if the anchor cell has a role in widening the basement membrane breach, we laser ablated the anchor cell at times before and after invasion and examined laminin::GFP (Fig. 2a,c). When the anchor cell was ablated just before invasion, the basement membrane remained completely intact through the L4 stage (Fig. 2a; 16/16 animals examined). Blocking invasion in animals expressing a dominant negative form of the *C. elegans* integrin specifically in the anchor cell (*zmp-1*>*HA- β -tail*; HA, haemagglutinin; ref. 33) also resulted in a failure to generate a basement membrane gap (20/20 animals). In contrast, basement membrane gap expansion was normal when the anchor cell was killed just after invasion (19/19 animals; Fig. 2c). We conclude that the anchor cell is required to initiate a breach in the basement membrane, but dispensable for basement membrane gap expansion.

The descendants of the ventral uterine cells limit basement membrane gap opening

The anchor cell ablation experiments suggested that neighbouring uterine or vulval cells regulate basement membrane gap opening once the anchor cell makes the initial breach. To investigate a possible role for the uterine cells, we first laser ablated the dorsal uterine cells³⁴. Removal of the dorsal uterine cells and their descendants did not alter the expansion or positioning of the basement membrane gap (Table 1; Fig. 2e). In contrast, laser ablation of the ventral uterine cells perturbed gap formation. Surprisingly, this alteration resulted in basement membrane gap boundaries overexpanding in nearly 20% of operated animals (moving beyond the vulD cell; the remaining animals had normal basement membrane gap positioning; Table 1; Fig. 2g). Thus, the ventral uterine cell descendants restrict basement membrane gap expansion.

The vulval cells promote basement membrane gap expansion

To determine if the vulval cells play a role in promoting basement membrane gap expansion, we first examined basement membrane opening in vulvaless animals (genotype *lin-3(n1059)/lin-3(n378)*; ref. 35), a condition where approximately 20% of anchor cells invade⁸. In these cases, we found that the basement membrane gap never extended beyond the anchor cell ($n = 10/10$ animals; Fig. 3a,b,e and Supplementary Movie S5). Similar results were observed in animals where vulval cell divisions were blocked with hydroxyurea ($n = 10/10$ animals; Fig. 3c,e; ref. 8). To further examine the role of the vulval cells in promoting basement membrane gap expansion, we reduced the number of VPCs by laser ablating all VPCs except the innermost P6.p descendants P6.pa and P6.pp, a treatment that does not interfere with anchor cell invasion and results in the isolated development of 1°-fated vulF cells (see Fig. 1a). This reduction of the number and invagination of VPCs decreased the expansion of the basement membrane gap (Fig. 3d,e). These results indicate that the vulval cells promote basement membrane gap expansion. Furthermore, the degree of basement membrane gap enlargement seems to be tied to vulval cell division or invagination.

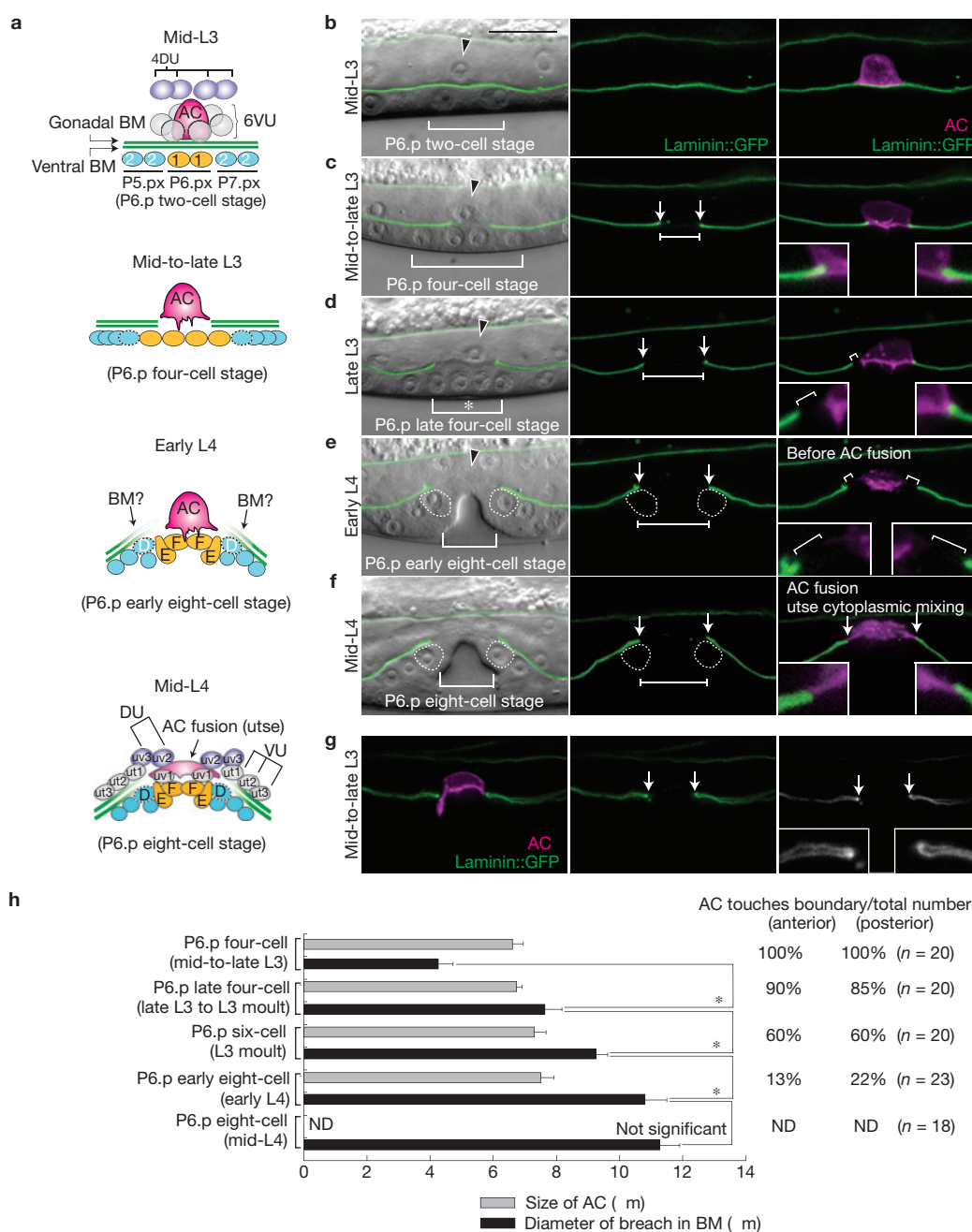


Figure 1 The gap in the basement membrane expands during uterine–vulval attachment. **(a)** Uterine–vulval attachment. At the late L3 larval stage, all of the VPCs (below the basement membrane) divide except for the 2°-fated vulD cells (dotted white line), as the anchor cell moves between the central 1°-fated VPCs (vulF cells) at the apex of the invaginating vulva. The fate of the basement membrane is unknown during the later phases of uterine–vulval attachment. (VU, ventral uterine cell; DU, dorsal uterine cell; AC, anchor cell; BM, basement membrane; D, vulD cells; E, vulE cells; F, vulF cells). **(b–f)** Anterior is left and ventral is down, black arrowheads indicate anchor cells and scale bars represent 10 μm in this and all subsequent figures. Differential interference contrast (DIC) images overlaid with basement membrane fluorescence (left) or fluorescent images show the uterine–vulval region of wild-type hermaphrodites. The anchor cell and basement membrane are labelled with mCherry::PLC δ^{PH} (magenta) and laminin::GFP (green), respectively. **(b)** At the mid-L3, intact basement membrane separates the uterine and vulval tissues and the anchor cell sits directly over the P6.p 1° VPC daughters (brackets). **(c)** By the mid-to-late L3 stage, anchor

cell invasion has generated a basement membrane gap (white arrows, boundary; white bar, diameter in this and all subsequent figures). At this time, the anchor cell is in contact with the basement membrane (right panel, insets). **(d)** During the late L3 stage, the central 1° VPCs invaginate (asterisk) and the basement membrane gap expands beyond the anchor cell (inverted bracket). **(e)** By the early L4 stage, the 1° VPCs have divided again and are out of the plane of focus. White dotted lines are the 2°-fated vulD cells. **(f)** The expanding gap stabilizes over the vulD cells (dotted white line in this and all subsequent figures) abutting the multinucleate utse cell (insets) by the mid-L4 stage. **(g)** Left, merged fluorescence; centre, basement membrane fluorescence; right, grey scale. After anchor cell invasion, separation of the uterine and vulval tissues revealed that the gonadal and ventral epidermal basement membranes fused bordering the site of invasion (white arrows, insets). **(h)** The diameter of the anchor cell and the basement membrane gap at each stage. The P6.p six-cell stage is when the outer P6.p granddaughters have divided. Asterisks denote statistically significant differences ($P < 0.05$; Student's t -test). Error bars represent s.e.m. ND, not determined.

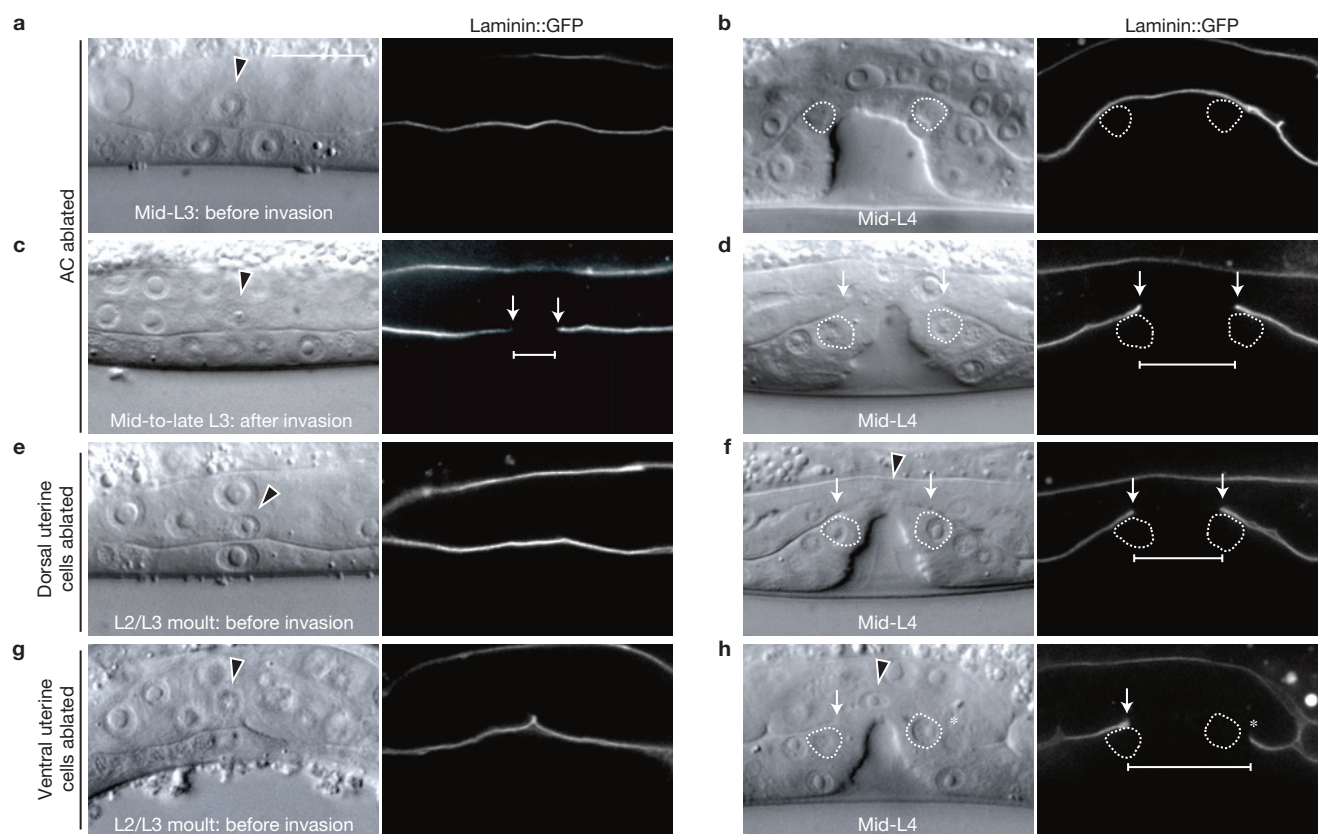


Figure 2 The role of the uterine cells during basement membrane gap formation. **(a,c,e,g)** DIC images (left) and corresponding confocal sections of basement membrane viewed with laminin::GFP (right) show animals before laser-directed cell ablation. **(b,d,f,h)** Similar images show corresponding animals after laser ablation at the mid-L4 stage. **(a)** When the anchor cell (AC) was killed by laser ablation just before invasion (P6.p two-cell stage), the basement membrane separating the uterine and vulval tissues remained intact later at the mid-L4 stage **(b)**. **(c)** When the anchor cell

was ablated just after invasion (P6.p four-cell stage), basement membrane gap expansion was normal **(d)**. **(e)** Laser ablation of the dorsal uterine cells that sit above the anchor cell at L2/L3 moult (P6.p one-cell stage) had no effect on uterine–vulval attachment or basement membrane gap formation **(f)**. **(g)** Ablation of the ventral uterine cells at L2/L3 moult resulted in an overexpansion of the basement membrane gap past the vulD cells in 20% of the basement membrane boundaries examined **(h)**; the asterisk indicates overexpansion at the posterior boundary.

Basement membrane sliding underlies gap expansion

Breaches in basement membrane that form during developmental processes and in tumorigenesis have been postulated to result from proteolytic dissolution or reduced basement membrane deposition⁵. To determine if proteolytic degradation underlies gap expansion, we first conducted an RNA interference (RNAi) screen, examining basement membrane gap expansion after RNAi-mediated knockdown of 260 of the 298 *C. elegans* genes with putative protease or protease inhibitor domains (Supplementary Table S1). No defects in basement membrane gap expansion, however, were observed (Supplementary Table S2). To further test a role for basement membrane dissolution, we established transgenic worms expressing laminin::Dendra and type IV collagen::Dendra. Dendra is a highly stable, photoconvertible fluorescent protein that changes from the green to red fluorescent state using low-phototoxic short-wavelength light³⁶. We converted a 5- μ m-wide segment of basement membrane at the edge of the forming gap at the P6.p four-cell stage (Fig. 4a and Supplementary Fig. S1) and followed this highlighted boundary basement membrane until the P6.p eight-cell stage. If dissolution accounted for gap expansion, we predicted that the optically highlighted boundary basement membrane would be removed. Instead, we found that the highlighted basement membrane was not lost, but rather shifted from

a location over the 1°-fated vulF cells to a position above the 2°-fated vulD cells (Fig. 4a; $n = 33/33$ animals examined). Measurements of the photoconverted basement membrane confirmed that it did not shrink during movement, but slightly expanded, possibly a result of laminin diffusion or the gonadal and ventral epidermal basement membranes shifting relative to each other (Fig. 4c). Notably, photoconversion of a small (approximately 1.25 μ m) region of laminin::Dendra at the basement membrane boundary never visibly separated during sliding ($n = 5/5$ animals), suggesting that the two basement membranes slid in register. We observed a decrease in fluorescence of the photoconverted laminin::Dendra; however, this was comparable to that of control regions and probably a result of photobleaching and basement membrane turnover (Fig. 4d). Similar results were obtained with type IV collagen::Dendra, suggesting that sliding is a property of this region of basement membrane (Supplementary Fig. S1).

To determine if reduced basement membrane deposition might also contribute to basement membrane gap expansion, we carried out landmark photobleaching with animals expressing laminin::GFP. Regions of the basement membrane bordering the expanding gap and at a distance were not different in fluorescence recovery after photobleaching (Supplementary Fig. S2). Thus, reduced basement membrane deposition does not contribute to gap widening.

Table 1 Basement membrane gap position during uterine–vulval attachment

Genotype/treatment	Basement membrane gap position*			
	P6.p early eight-cell stage (early L4 stage)		P6.p eight-cell stage (mid-L4 stage)	
	Percentage of expanded gap boundary*	n =	Percentage of expanded gap boundary*	n =
Wild type (N2)	0.0	100	3.0	100
Cell ablation				
Anchor cell ablation at P6.p two-cell stage; wild type (N2)	ND	16	Basement membrane intact	16
Anchor cell ablation at P6.p early four-cell stage; wild type (N2)	ND		0	60
Three ventral uterine cells ablation; wild type (N2)	ND		19.4	62
Two dorsal uterine cells ablation; wild type (N2)	ND		1.9	54
Integrin				
<i>ina-1(gm39)</i>	6.0	100	13.0	100
<i>qyls110[egl-17>HA-β-tail]</i> †	5.0	60	22.2	90
<i>ina-1</i> (RNAi); <i>qyls138[unc-62>rde-1]; rde-1(ne219); rrf-3(pk1426)</i> ‡	8.8	80	19	100
<i>pat-2</i> (RNAi); <i>qyls138[unc-62>rde-1]; rde-1(ne219); rrf-3(pk1426)</i> ‡	1	100	4	100
<i>pat-3</i> (RNAi); <i>qyls138[unc-62>rde-1]; rde-1(ne219); rrf-3(pk1426)</i> ‡	5.8	70	17.4	80
<i>ina-1</i> (RNAi); <i>qyls103[fos-1a>rde-1]; rde-1(ne219); rrf-3(pk1426)</i> ‡	1.7	60	5	80
<i>pat-2</i> (RNAi); <i>qyls103[fos-1a>rde-1]; rde-1(ne219); rrf-3(pk1426)</i> ‡	0	60	3.8	80
<i>pat-3</i> (RNAi); <i>qyls103[fos-1a>rde-1]; rde-1(ne219); rrf-3(pk1426)</i> ‡	1.7	60	4.5	90
<i>vab-19</i>				
<i>vab-19(e1036)</i> §	2.5	80	7.8	90
<i>vab-19</i> (RNAi); <i>qyls138[unc-62>rde-1]; rde-1(ne219); rrf-3(pk1426)</i> ‡	5.6	90	12.5	90
<i>vab-19</i> (RNAi); <i>qyls103[fos-1a>rde-1]; rde-1(ne219); rrf-3(pk1426)</i> ‡	0	60	3.3	90
Pathway interactions				
<i>vab-19(e1036); qyls110[egl-17>HA-η-tail]</i> §	6.3	80	31.3	80
Three ventral uterine cells ablation; <i>qyls110[egl-17>HA-β-tail]</i>	ND		79.5	64
Three ventral uterine cells ablation; <i>vab-19(e1036)</i> §	ND		56.7	60

*Gap expansion was scored by the position of anterior and posterior boundaries in relation to the vulD cell under DIC optics. The basement membrane boundary in wild-type animals is located over the vulD cell at the P6.p eight-cell stage during the early and mid-L4 stage of development. Expanded gaps in the basement membrane boundary were scored as extending beyond the vulD cell. †Two other transgenic lines showed similar results. ‡The *rrf-3* mutant background is more sensitive to somatic RNAi effects. §The cold-sensitive mutant *vab-19(e1036)* was scored at 17 °C. Wild-type basement membrane gap positioning was normal at this temperature. ND = not determined.

To examine if the sliding basement membrane is compressed during gap expansion, we photoconverted alternating 5-μm-wide stripes of laminin::Dendra adjacent to the expanding basement membrane gap. These stripes were not compressed and shifted in relation to the underlying vulval cells (Fig. 4b,e and Supplementary Fig. S1). During the time of basement membrane gap expansion, we found that the vulval and uterine tissue nearly doubled in size (1.7- and 2.0-fold, respectively), suggesting that the displaced basement membrane was spreading over the growing tissues. Taken together, these results indicate that basement membrane shifting underlies gap expansion during uterine–vulval attachment.

Vulval expressed INA-1/PAT-3 (integrin) restricts basement membrane gap expansion

To determine the molecular mechanisms that regulate basement membrane gap formation, we conducted a focused screen and examined 15 strains containing mutant alleles of genes encoding secreted and transmembrane proteins whose RNAi knockdown leads to uterine–vulval attachment defects (WormBase Release WS210; Supplementary Table S3). We found that animals harbouring a hypomorphic mutation in one of these genes, coding for the integrin α-subunit *ina-1* (*gm39*; ref. 37), had a weakly penetrant basement membrane gap positioning defect, with 13% of observed gaps showing an overexpanded boundary at the mid-L4 stage (Fig. 5a; Table 1). Integrin receptors are composed of a single α and β-subunit and mediate cell–matrix interactions³⁸. *C. elegans* possess two integrin receptors, consisting of the α-subunits INA-1 (similar to vertebrate laminin-binding integrins) or PAT-2 (similar to vertebrate

RGD-binding integrins) bound with the lone β-subunit, PAT-3 (ref. 32). As null alleles in all of these genes lead to embryonic or early larval lethality, we used vulval- (*unc-62>rde-1*) and uterine-specific (*fes-1a>rde-1*) RNAi strains to further examine their functions^{13,33}. RNAi-targeted depletion of *ina-1*, *pat-2* or *pat-3* in the uterine tissue (*fes-1a>rde-1* strain) did not significantly alter basement membrane gap positioning (Table 1). RNAi-targeted knockdown of *ina-1* and *pat-3* in the vulval tissue (*unc-62>rde-1* strain), however, caused an overexpansion defect, similar to *ina-1(gm39)* mutants (Table 1). No defects in basement membrane gap formation were observed after RNAi depletion of *pat-2* in the vulval tissue (Table 1). These results suggest that the INA-1/PAT-3 heterodimer functions in the vulval cells to restrict basement membrane gap opening.

Similar to *Drosophila* and vertebrate cells, we have found that α- and β-integrin subunits require heterodimerization within the secretory apparatus of the uterine and vulval cells to be transported efficiently to the cell surface^{33,39,40}. We thus examined the localization of a full-length PAT-3::GFP construct co-transformed with genomic DNA encoding INA-1 or PAT-2 (ref. 33). Co-transformation of *pat-3::GFP* with *ina-1* showed enriched PAT-3::GFP localization at the site of the basement membrane gap boundary position during the mid-L4 stage (Fig. 5b–d). Mosaic expression studies indicated that the boundary-localized INA-1/PAT-3::GFP was derived from the vulval cells, most strongly within the vulD cells (Supplementary Fig. S3). Consistent with a function here, expression of a dominant negative integrin β-subunit PAT-3 construct in the vulD and neighbouring vulC cells driven by the *egl-17* promoter (*egl-17>HA-β-tail*) resulted in a basement membrane gap overexpansion defect (Table 1). Neither

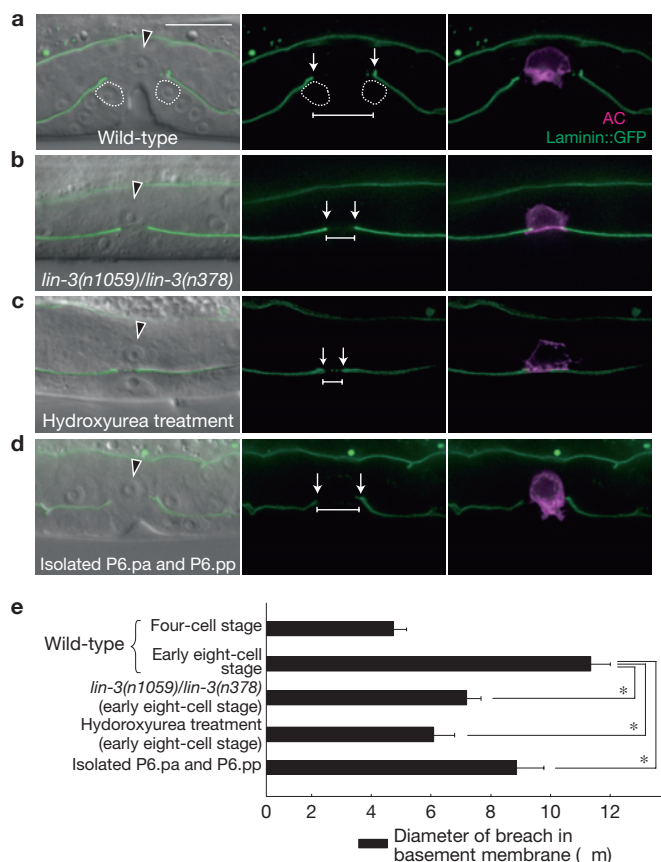


Figure 3 The VPCs expand the breach in the basement membrane. (a–d) DIC images overlaid with confocal sections of basement membrane labelled with laminin::GFP (green, left) and confocal microscopy images of basement membrane fluorescence alone (middle) and an anchor cell (AC, expressing *cdh-3>mCherry::PLCδ^{PH}*, magenta) with basement membrane (right) in early-L4-stage animals. (a) By the early L4 stage in wild-type animals (P6.p early eight-cell stage), the basement membrane gap had expanded and stabilized over the vulD cells. (b) When the anchor cell invaded in a vulvaless animal (*lin-3(n1059)/lin-3(n378)*), the gap that formed in the basement membrane never expanded beyond the anchor cell. (c) Similarly, when vulval cell division was blocked by hydroxyurea treatment, the basement membrane gap never expanded beyond the anchor cell. (d) Laser-directed killing of all VPCs, except P6.pa and P6.pp, which give rise to the vulF cells (see Fig. 1a), resulted in a reduction in basement membrane gap enlargement. (e) The average diameter of the breach generated in the basement membrane in wild-type, vulvaless and hydroxyurea-treated animals and isolated P6.pa and P6.pp cells ($n = 10$ animals examined for each treatment). The asterisks denote a statistically significant difference ($P < 0.05$; Student's *t*-test). Error bars represent s.e.m.

ina-1(gm39) nor *egl-17>HA-β-tail* animals had alterations in vulval fate specification (Supplementary Fig. S4), supporting a direct role for INA-1/PAT-3 in limiting basement membrane gap expansion. No significant concentrations of PAT-2/PAT-3::GFP integrin were detected in the vulval or uterine cells participating in boundary formation³³. These studies indicate that vulval-localized INA-1/PAT-3 integrin limits basement membrane gap expansion.

Vulval VAB-19 (Kank) stabilizes basement membrane gap position

In a screen for genes expressed during uterine–vulval attachment, we found that a full-length GFP-tagged expression construct for the

protein VAB-19, a homologue of the cytoplasmic tumour-suppressor protein Kank²⁶, localized to the site of the basement membrane gap boundary (Fig. 5f–h). VAB-19 regulates epithelial cell–matrix attachment structures in the *C. elegans* embryo^{25,41}, suggesting that it might participate in basement membrane gap positioning during uterine–vulval attachment. Null mutations in *vab-19* are embryonic lethal⁴¹. Thus, we examined basement membrane boundary position in the cold-sensitive mutant *vab-19(e1036)* (ref. 41) and found a weakly penetrant defect at a restrictive temperature of 17 °C, with 8% of observed basement membrane boundaries overexpanded (Fig. 5e; Table 1). Similar to integrin function, vulval- and uterine-specific RNAi-mediated knockdown of *vab-19* suggested that *vab-19* functions within the vulval cells (Table 1). Mosaic expression analysis revealed that VAB-19::GFP was also expressed most strongly in the vulD cells at the basement membrane gap boundary, and weakly expressed in the uterine cells (Supplementary Fig. S3). To explore the interaction between integrin and VAB-19 function, we examined *vab-19(e1306)* mutant animals harbouring the vulval-expressed dominant negative integrin *egl-17>HA-β-tail* and found an additive defect in basement membrane gap hyperexpansion (Table 1). These results indicate that integrin and VAB-19 function together, in either the same or parallel pathways, to limit basement membrane gap expansion within the vulval cells.

Vulval and uterine cells function together to limit basement membrane gap expansion

Our data show that VAB-19 and INA-1/PAT-3 function within the vulval cells, in combination with an additional mechanism in the ventral uterine cell descendants, to restrict basement membrane gap expansion. To explore the interaction between these mechanisms, we carried out ventral uterine cell ablation in *egl-17>HA-β-tail* (vulD-expressed dominant negative integrin) animals and found a strong synergistic interaction. Whereas *egl-17>HA-β-tail* and ventral uterine cell ablation each resulted in approximately 20% of basement membrane boundaries showing an overexpanded position, the combined perturbations resulted in 80% of basement membrane gap borders being hyperexpanded (Table 1; Fig. 6a–c). Similarly, we observed a robust synergistic interaction in *vab-19(e1306)* animals after ventral uterine cell ablation to nearly 60% of basement membrane gap boundaries being overexpanded (Table 1). Importantly, vulval cell division and invagination seemed normal in these animals. Measurements of vulval height and width after reductions of VAB-19 and integrin function revealed no differences when compared with wild-type animals (Supplementary Fig. S5), consistent with integrin and VAB-19 functioning directly to limit the sliding of the basement membrane, rather than indirectly through alterations in vulval morphogenesis. Taken together, these data support a cooperative function for VAB-19 (Kank) and INA/PAT-3 (integrin) within the vulval cells and a distinct molecular mechanism operating in the ventral uterine cell descendants that acts to limit basement membrane movement during uterine–vulval attachment.

DISCUSSION

How cells create gaps in basement membrane during normal morphogenetic and pathogenic processes is poorly understood^{4,6}. Using uterine–vulval attachment in *C. elegans* as a model for basement

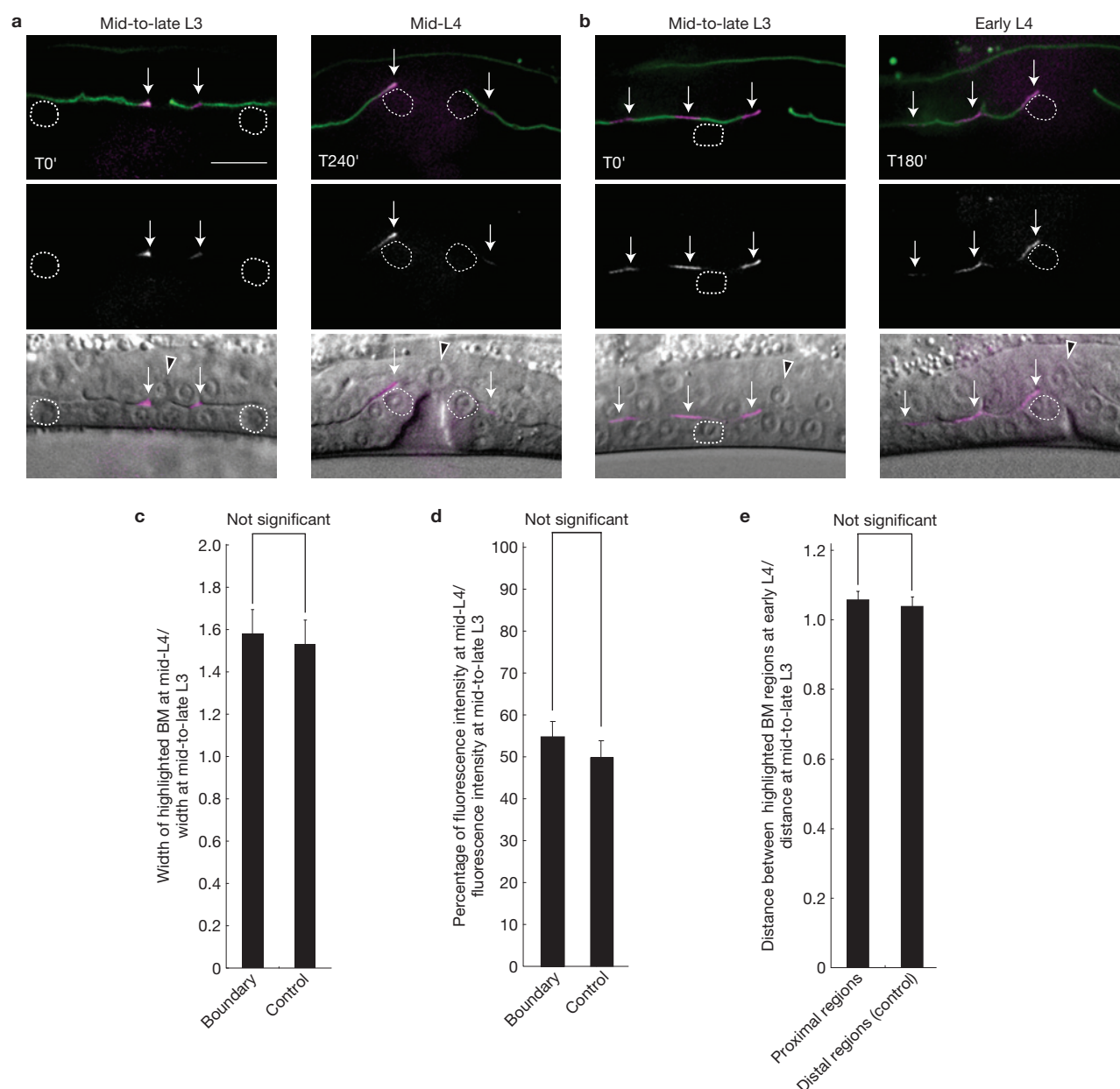


Figure 4 Basement membrane sliding underlies basement membrane gap enlargement. **(a,b)** Fluorescence overlays show laminin::Dendra after localized exposure to 405 nm light (white arrows point to optically highlighted (photoconverted) regions of laminin::Dendra, shown in magenta; top). Corresponding images show only photoconverted laminin::Dendra (middle, grey scale) and laminin::Dendra overlaid on DIC (bottom, magenta). Times are shown in minutes; T0' is the time at which the laminin::Dendra was first photoconverted. **(a)** Left: two 5- μ m-wide regions of laminin::Dendra were photoconverted; one at the anterior boundary of the gap and a second region several micrometres posterior to the gap (control). Right: the same animal as shown on the left, 240 min later. The photoconverted region of laminin::Dendra was not lost and shifted from a location over the vulF precursor cell to occupy a position over the vulD cell ($n = 33/33$ animals).

(b) Left: three regions of laminin::Dendra were photoconverted; one at the edge of the basement membrane (BM) gap, and two at distances anterior to the gap. Right: the animal shown on the left, 180 min later. **(c)** Quantification of the width of the regions at the mid-L4 stage, compared with the width of the regions at the mid-to-late L3 stage (the detailed method is shown in Supplementary Fig. S1). **(d)** Average ratio of fluorescence intensity at mid-L4, compared with the fluorescence intensity at time of photoconversion during the mid-to-late L3. **(e)** Quantification of the ratio of the distance between the regions at the early L4 stage to the distance between the regions at the mid-to-late L3 (the detailed method is shown in Supplementary Fig. S1; $n = 10$ animals for each experiment). No statistical differences between experimental and control highlighted regions were observed ($P > 0.05$, Student's t -test). Error bars represent s.e.m.

membrane remodelling, we show that, after the uterine anchor cell breaches the basement membrane, the underlying vulval cells expand and then stabilize the basement membrane gap by promoting basement membrane sliding followed by targeted adhesion at a specific cellular boundary (summarized in Fig. 6d,e). This *in vivo* work reveals that

a previously unknown mechanism, basement membrane sliding, underlies basement membrane gap enlargement and highlights how collaborative interactions between an invasive cell and the tissue invaded can open basement membrane breaches. Notably, cooperative interactions between leukocytes and endothelial cells are thought to

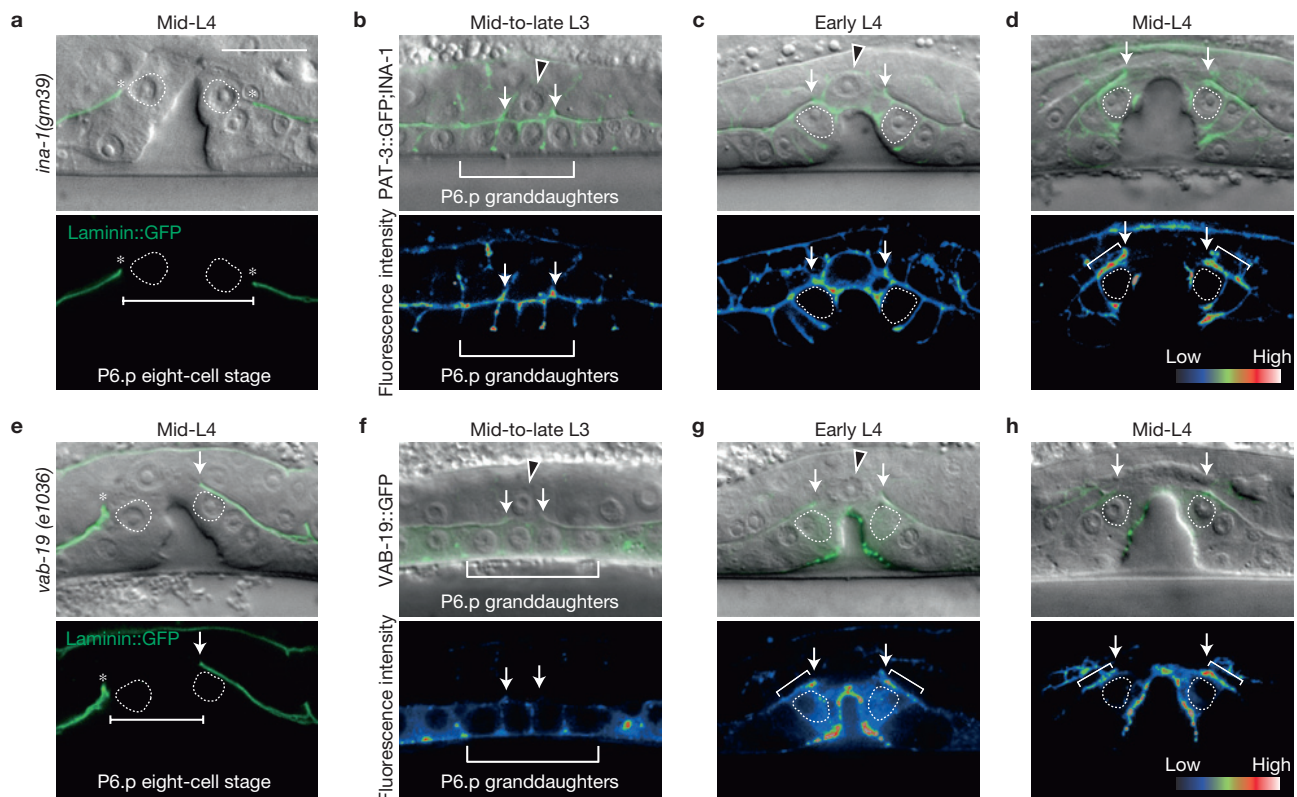


Figure 5 INA-1/PAT-3 (integrin) and VAB-19 (Kank) stabilize the basement membrane gap boundary. **(a,e)** DIC images overlaid with basement membrane fluorescence (labelled with laminin::GFP, upper) and basement membrane fluorescence images alone (lower). **(b-d,f-h)** DIC images overlaid with PAT-3::GFP and VAB-19::GFP fluorescence (green; upper), and corresponding spectral representations of the fluorescence intensity (lower). **(a)** An *ina-1(gm39)* mutant where the gap in the basement membrane has expanded beyond the vulD cells (asterisks). **(b-d)** PAT-3::GFP was expressed throughout the uterine and vulval

tissues at the mid-to-late L3 stage and became enriched (inverted brackets) at the boundary of the basement membrane gap (arrows) by the mid-L4 stage ($n = 51/60$ animals examined). **(e)** A *vab-19(e1036)* mutant where the gap in the basement membrane has overexpanded on the anterior side (asterisk). **(f-h)** VAB-19::GFP localized to sites of cell-cell contact within the uterine and vulval tissues at mid-to-late L3 **(f)** and became enriched (inverted brackets) at the boundary of the gap in basement membrane at the early and mid-L4 larval stages ($n = 57/60$ animals; **g,h**).

promote leukocyte passage through endothelial basement membrane (refs 5,6,42). Such collaborative interplay may be a common strategy to form basement membrane gaps.

Proteolytic degradation or reduced basement membrane assembly are postulated mechanisms underlying basement membrane gap formation¹. The fate of the basement membrane lost during these events, however, has not been determined, and thus the mechanisms that promote removal remain unclear. By following the fate of the basement membrane through optical highlighting of laminin::Dendra and type IV collagen::Dendra, we show that the basement membrane is not removed by dissolution during uterine–vulval attachment. Further, landmark photobleaching of laminin::GFP revealed no reduction in basement membrane deposition at the expanding gap boundary. Instead, our optical highlighting experiments demonstrate that the basement membrane shifts to expand the gap. As the basement membrane slides at the boundary, the juxtaposed uterine and vulval cells make direct cell–cell connections²⁷, which probably excludes further basement membrane deposition. During uterine–vulval attachment the uterine and vulval tissue nearly double in size, supplying the sliding basement membrane with enlarged tissue to spread over. Tissue growth might be a prerequisite for basement membrane sliding, providing a surface for the shifted basement membrane to cover.

Proteases may also be used to facilitate basement membrane sliding; however, our optical highlighting experiments clearly show that these do not dissolve the basement membrane. Notably, proteolysis might be particularly important in initiating the break in the basement membrane, as the *C. elegans* matrix metalloproteinase encoded by *zmp-1* is expressed within the anchor cell during invasion and is thought to function during the initial breaching event²¹. The reliance of basement membrane sliding on the number of dividing and invaginating vulval cells suggests that these morphogenetic processes provide the force to move the basement membrane, analogous to migrating fibroblasts shifting collagen fibres in connective-tissue matrix⁴³. Importantly, the basement membrane sliding model does not preclude an active role for the vulval cells in expanding the gap by migrating into the opening (as opposed to basement membrane sliding over them). However, as vulval morphogenesis was normal in cases with overexpanded borders, we propose basement membrane sliding as the primary mechanism driving basement membrane gap expansion.

Our studies indicate that, after the invaginating vulval cells initiate basement membrane sliding, the uterine and vulval cells have independent mechanisms for halting this movement at a specific cellular boundary. Laser ablation of the ventral uterine cells increased the expansion of the basement membrane gap,

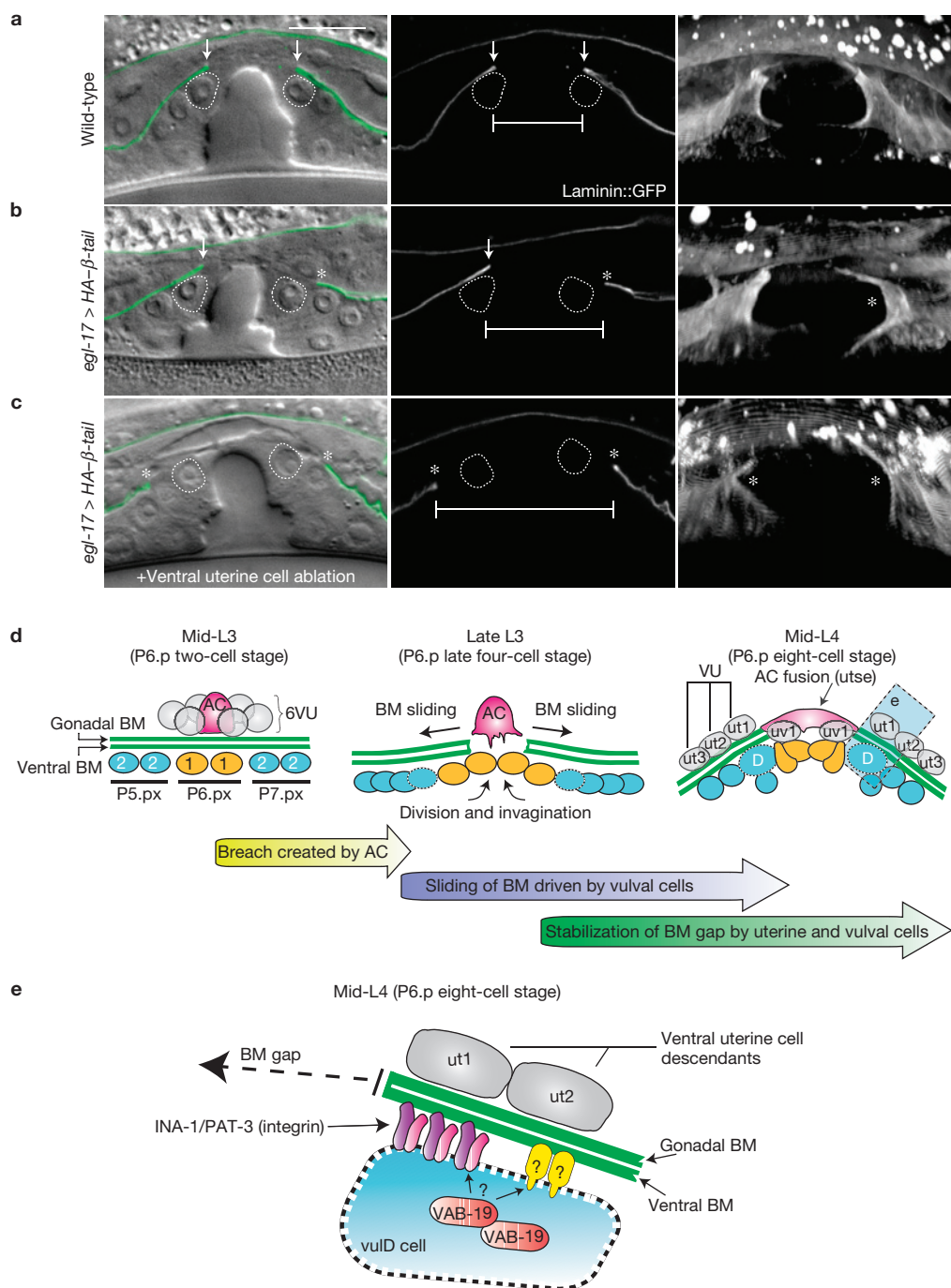


Figure 6 The uterine and vulval cells act together to limit basement membrane gap expansion. (a–c) DIC overlaid with basement membrane fluorescence (labelled with laminin::GFP, green, left), grey scale of basement membrane fluorescence (middle) and corresponding three-dimensional reconstruction of an entire confocal z-stack of the basement membrane fluorescence (right, rotated 45° forward). (a) In wild-type animals, the boundary of the gap in the basement membrane stabilized over the vulD cells. (b) Expression of a dominant negative PAT-3 β -integrin construct (*HA- β -tail*) in the vulD cells (*egl-17 > HA- β -tail*) caused overexpansion of the final position of the posterior basement membrane gap boundary (asterisk) at the mid-L4 larval stage, also seen in the three-dimensional reconstruction (right). (c) Ventral uterine cell ablation in animals expressing the HA- β -tail construct within the vulD cells resulted in a stronger overexpansion defect than either perturbation alone. (d) A schematic diagram depicting three stages of basement membrane

gap formation during uterine–vulval attachment. At the mid-L3 larval stage the uterine and vulval tissues are separated by the ventral and gonadal basement membranes. The anchor cell initiates the breach in the basement membrane at the mid-to-late L3 larval stage. Following anchor cell invasion, the dividing and invaginating vulval cells promote basement membrane sliding to expand the basement membrane gap (arrows). At the early-to-mid-L4 stage basement membrane sliding is halted over the vulD cells by INA-1/PAT-3 and VAB-19 activity within the vulD cells, and a distinct adhesion mechanism that functions within the ventral uterine cell descendants. (VU, ventral uterine cell; AC, anchor cell; BM, basement membrane; D, vulD cells.) (e) An enlarged view of the attachment site shows INA-1/PAT-3 and VAB-19 as well as the ventral uterine descendant ut1 and ut2 cells stabilizing the boundary of the gap that forms in the basement membrane. VAB-19 may function with integrin or an alternative protein that binds to basement membrane.

demonstrating that these cells act to restrict basement membrane movement. Furthermore, the expression patterns and loss-of-function phenotypes of the genes encoding the integrin heterodimer INA-1/PAT-3 and the Kank homolog VAB-19 indicate that these proteins act in the vulval vulD cells to limit basement membrane gap expansion (Fig. 6e). The INA-1/PAT-3 integrin heterodimer is most similar to vertebrate integrin laminin receptors³⁷, consistent with a role in cell–basement membrane adhesion. Although the *in vivo* functions of Kank proteins are poorly understood, VAB-19/Kank has also previously been implicated in mediating cell–basement membrane interactions in *C. elegans*^{25,41}. VAB-19 is thought to act as a cytoskeletal linker with the transmembrane protein Myotactin/LET-805 within the epidermis to bind basement membrane, whereas integrin acts within the muscle cells to bind basement membrane, thus forming a mechanical linkage between muscle and the cuticle^{44,45}. Our experiments demonstrate another example where VAB-19 and integrin act cooperatively during an attachment process. Neither integrin nor VAB-19 seems to function or be expressed strongly in the uterine cells, suggesting that these cells use a distinct adhesion mechanism to restrict basement membrane sliding. Such an intricate boundary-positioning system probably ensures robust opening of the basement membrane gap without disrupting tissue integrity.

Although basement membranes have been hypothesized to be highly static structures^{46–48}, there have been few real-time analysis studies of basement membrane dynamics *in vivo*. Recent work examining chick primitive-streak formation has shown that the underlying subepiblastic extracellular matrix (a matrix similar to basement membrane) moves with the migrating epiblastic cells⁴⁹. Our observations demonstrating that the basement membrane is shifted during gap expansion in uterine–vulval development in *C. elegans* provide further evidence that basement membrane itself can have plastic properties. Similar to uterine–vulval development, the formation of basement membrane gaps during vertebrate gastrulation and *Drosophila* disc eversion and in metastatic tumours^{7,9,50} is associated with dividing and moving cells, where similar conditions to shift basement membrane probably occur. Thus, basement membrane sliding may be a common strategy to widen basement membrane gaps, with important implications for the design of therapies to modulate this behaviour. □

METHODS

Methods and any associated references are available in the online version of the paper at <http://www.nature.com/naturecellbiology>

Note: Supplementary Information is available on the Nature Cell Biology website

ACKNOWLEDGEMENTS

We are grateful to A. Chisholm for the *vab-19::GFP* vector; J. Culotti for the *mig-6(ev700)* strain; J. Schwarzbauer for the *pat-3* HA- β -tail vector; S. Mitani for the deletion mutant (*tm1291*), S. Johnson of the Duke University LMCF for imaging advice, the *Caenorhabditis* Genetic Center for strains, and A. Schindler, D. Matus and L. Lilley for comments on the manuscript. This work was supported by a Basil O'Connor Scholars Research Award, The Pew Scholars Program in the Biomedical Sciences and NIH grants GM079320 and GM079320-03S1 to D.R.S., HD027211 to J.M.K. and a JSPS Postdoctoral Fellow for Research Abroad Award to S.I.

AUTHOR CONTRIBUTIONS

S.I. carried out most of the experiments. All other authors carried out particular subsets of experiments or developed key reagents. D.R.S. and S.I. designed the project and D.R.S., S.I., E.J.H. and M.A.M. wrote the manuscript.

COMPETING FINANCIAL INTERESTS

The authors declare no competing financial interests.

Published online at <http://www.nature.com/naturecellbiology>

Reprints and permissions information is available online at <http://www.nature.com/reprints>

- Rowe, R. G. & Weiss, S. J. Navigating ECM barriers at the invasive front: the cancer cell–stroma interface. *Annu. Rev. Cell Dev. Biol.* **25**, 567–595 (2009).
- Sherwood, D. R. Cell invasion through basement membranes: an anchor of understanding. *Trends Cell Biol.* **16**, 250–256 (2006).
- Kalluri, R. Basement membranes: structure, assembly and role in tumour angiogenesis. *Nat. Rev. Cancer* **3**, 422–433 (2003).
- Even-Ram, S. & Yamada, K. M. Cell migration in 3D matrix. *Curr. Opin. Cell Biol.* **17**, 524–532 (2005).
- Rowe, R. G. & Weiss, S. J. Breaching the basement membrane: who, when and how? *Trends. Cell Biol.* **18**, 560–574 (2008).
- Nourshargh, S., Hordijk, P. L. & Sixt, M. Breaching multiple barriers: leukocyte motility through venular walls and the interstitium. *Nat. Rev. Mol. Cell Biol.* **11**, 366–378 (2010).
- Nakaya, Y., Sukowati, E. W., Wu, Y. & Sheng, G. RhoA and microtubule dynamics control cell–basement membrane interaction in EMT during gastrulation. *Nat. Cell Biol.* **10**, 765–775 (2008).
- Sherwood, D. R. & Sternberg, P. W. Anchor cell invasion into the vulval epithelium in *C. elegans*. *Dev. Cell* **5**, 21–31 (2003).
- Srivastava, A., Pastor-Pareja, J. C., Igaki, T., Pagliarini, R. & Xu, T. Basement membrane remodeling is essential for *Drosophila* disc eversion and tumour invasion. *Proc. Natl Acad. Sci. USA* **104**, 2721–2726 (2007).
- Barsky, S. H., Siegal, G. P., Jannotta, F. & Liotta, L. A. Loss of basement membrane components by invasive tumours but not by their benign counterparts. *Lab. Invest.* **49**, 140–147 (1983).
- Flug, M. & Kopf-Maier, P. The basement membrane and its involvement in carcinoma cell invasion. *Acta. Anat. (Basel)* **152**, 69–84 (1995).
- Frei, J. V. The fine structure of the basement membrane in epidermal tumours. *J. Cell Biol.* **15**, 335–342 (1962).
- Matus, D. Q. *et al.* *In vivo* identification of regulators of cell invasion across basement membranes. *Sci. Signal.* **3**, ra35 (2010).
- Spaderna, S. *et al.* A transient, EMT-linked loss of basement membranes indicates metastasis and poor survival in colorectal cancer. *Gastroenterology* **131**, 830–840 (2006).
- Cavallo-Medved, D. *et al.* Live-cell imaging demonstrates extracellular matrix degradation in association with active cathepsin B in caveolae of endothelial cells during tube formation. *Exp. Cell Res.* **315**, 1234–1246 (2009).
- Garbisa, S., Kniska, K., Tryggvason, K., Foltz, C. & Liotta, L. A. Quantitation of basement membrane collagen degradation by living tumour cells *in vitro*. *Cancer Lett.* **9**, 359–366 (1980).
- Hotary, K., Li, X. Y., Allen, E., Stevens, S. L. & Weiss, S. J. A cancer cell metalloprotease triad regulates the basement membrane transmigration program. *Genes Dev.* **20**, 2673–2686 (2006).
- Overall, C. M. & Kleifeld, O. Tumour microenvironment—opinion: validating matrix metalloproteinases as drug targets and anti-targets for cancer therapy. *Nat. Rev. Cancer* **6**, 227–239 (2006).
- Page-McCaw, A., Ewald, A. J. & Werb, Z. Matrix metalloproteinases and the regulation of tissue remodelling. *Nat. Rev. Mol. Cell Biol.* **8**, 221–233 (2007).
- Sameni, M., Dosescu, J., Yamada, K. M., Sloane, B. F. & Cavallo-Medved, D. Functional live-cell imaging demonstrates that β 1-integrin promotes type IV collagen degradation by breast and prostate cancer cells. *Mol. Imaging* **7**, 199–213 (2008).
- Sherwood, D. R., Butler, J. A., Kramer, J. M. & Sternberg, P. W. FOS-1 promotes basement-membrane removal during anchor-cell invasion in *C. elegans*. *Cell* **121**, 951–962 (2005).
- Xu, J. *et al.* Proteolytic exposure of a cryptic site within collagen type IV is required for angiogenesis and tumor growth *in vivo*. *J. Cell Biol.* **154**, 1069–1079 (2001).
- Liotta, L. A., Rao, N. C., Barsky, S. H. & Bryant, G. The laminin receptor and basement membrane dissolution: role in tumour metastasis. *Ciba. Found. Symp.* **108**, 146–162 (1984).
- Newman, A. P. & Sternberg, P. W. Coordinated morphogenesis of epithelia during development of the *Caenorhabditis elegans* uterine–vulval connection. *Proc. Natl Acad. Sci. USA* **93**, 9329–9333 (1996).
- Ding, M. *et al.* The cell signalling adaptor protein EPS-8 is essential for *C. elegans* epidermal elongation and interacts with the ankyrin repeat protein VAB-19. *PLoS One* **3**, e3346 (2008).
- Kakinuma, N., Zhu, Y., Wang, Y., Roy, B. C. & Kiyama, R. Kank proteins: structure, functions and diseases. *Cell Mol. Life Sci.* **66**, 2651–2659 (2009).
- Newman, A. P., White, J. G. & Sternberg, P. W. Morphogenesis of the *C. elegans* hermaphrodite uterus. *Development* **122**, 3617–3626 (1996).
- Lints, R. & Hall, D. H. Reproductive system, egg-laying apparatus. *WormAtlas* doi:10.3908/wormatlas.1.24 (2010).

29. Kao, G., Huang, C. C., Hedgecock, E. M., Hall, D. H. & Wadsworth, W. G. The role of the laminin beta subunit in laminin heterotrimer assembly and basement membrane function and development in *C. elegans*. *Dev. Biol.* **290**, 211–219 (2006).
30. Ziel, J. W., Hagedorn, E. J., Audhya, A. & Sherwood, D. R. UNC-6 (netrin) orients the invasive membrane of the anchor cell in *C. elegans*. *Nat. Cell Biol.* **11**, 183–189 (2009).
31. Fitzgerald, M. C. & Schwarzbauer, J. E. Importance of the basement membrane protein SPARC for viability and fertility in *Caenorhabditis elegans*. *Curr. Biol.* **8**, 1285–1288 (1998).
32. Kramer, J. M. Basement membranes. *WormBook* 1–15 (2005).
33. Hagedorn, E. J. *et al.* Integrin acts upstream of netrin signalling to regulate formation of the anchor cell's invasive membrane in *C. elegans*. *Dev. Cell* **17**, 187–198 (2009).
34. Kimble, J. & Hirsh, D. The postembryonic cell lineages of the hermaphrodite and male gonads in *Caenorhabditis elegans*. *Dev. Biol.* **70**, 396–417 (1979).
35. Liu, J., Tzou, P., Hill, R. J. & Sternberg, P. W. Structural requirements for the tissue-specific and tissue-general functions of the *Caenorhabditis elegans* epidermal growth factor LIN-3. *Genetics* **153**, 1257–1269 (1999).
36. Gurskaya, N. G. *et al.* Engineering of a monomeric green-to-red photoactivatable fluorescent protein induced by blue light. *Nat. Biotechnol.* **24**, 461–465 (2006).
37. Baum, P. D. & Garriga, G. Neuronal migrations and axon fasciculation are disrupted in *ina-1* integrin mutants. *Neuron* **19**, 51–62 (1997).
38. Yurchenco, P. D., Amenta, P. S. & Patton, B. L. Basement membrane assembly, stability and activities observed through a developmental lens. *Matrix Biol.* **22**, 521–538 (2004).
39. Leptin, M., Bogaert, T., Lehmann, R. & Wilcox, M. The function of PS integrins during *Drosophila* embryogenesis. *Cell* **56**, 401–408 (1989).
40. Marlin, S. D., Morton, C. C., Anderson, D. C. & Springer, T. A. LFA-1 immunodeficiency disease. Definition of the genetic defect and chromosomal mapping of alpha and beta subunits of the lymphocyte function-associated antigen 1 (LFA-1) by complementation in hybrid cells. *J. Exp. Med.* **164**, 855–867 (1986).
41. Ding, M., Goncharov, A., Jin, Y. & Chisholm, A. D. *C. elegans* ankyrin repeat protein VAB-19 is a component of epidermal attachment structures and is essential for epidermal morphogenesis. *Development* **130**, 5791–5801 (2003).
42. Madsen, C. D. & Sahai, E. Cancer dissemination—lessons from leukocytes. *Dev. Cell* **19**, 13–26 (2010).
43. Wolf, K. *et al.* Multi-step pericellular proteolysis controls the transition from individual to collective cancer cell invasion. *Nat. Cell Biol.* **9**, 893–904 (2007).
44. Altun, Z. F. & Hall, D. H. Muscle system, somatic muscle. *WormAtlas* doi:10.3908/wormatlas.1.7, (2009).
45. Cox, E. A., Tuskey, C. & Hardin, J. Cell adhesion receptors in *C. elegans*. *J. Cell Sci.* **117**, 1867–1870 (2004).
46. Leardkamolkarn, V. & Abrahamson, D. R. Binding of intravenously injected antibodies against laminin to developing and mature endocrine glands. *Cell Tissue Res.* **251**, 171–181 (1988).
47. Price, R. G. & Spiro, R. G. Studies on the metabolism of the renal glomerular basement membrane. Turnover measurements in the rat with the use of radiolabelled amino acids. *J. Biol. Chem.* **252**, 8597–8602 (1977).
48. Trier, J. S., Allan, C. H., Abrahamson, D. R. & Hagen, S. J. Epithelial basement membrane of mouse jejunum. Evidence for laminin turnover along the entire crypt–villus axis. *J. Clin. Invest.* **86**, 87–95 (1990).
49. Zamir, E. A., Rongish, B. J. & Little, C. D. The ECM moves during primitive streak formation—computation of ECM versus cellular motion. *PLoS Biol.* **6** e247 (2008).
50. Hanahan, D. & Weinberg, R. A. The hallmarks of cancer. *Cell* **100**, 57–70 (2000).

METHODS

Strains and culture conditions. Culturing and handling of *C. elegans* was done as previously described⁵¹. Wild-type animals were strain N2. In the text and figures, we designate linkage to a promoter with a > symbol and use a :: symbol for linkages that fuse open reading frames. The following alleles and transgenes were used in this study: *qyEx36[pat-3::GFP; genomic ina-1]*, *qyEx76[vab-19::GFP]*, *qyEx43[pat-3::GFP; genomic pat-2]*, *qyIs103[fos-1a>rde-1]*, *qyIs110[egl-17>HA-β-tail]*, *qyIs111[egl-17>HA-β-tail]*, *qyIs138[unc-62>rde-1]*, *qyIs139[unc-62>rde-1]*, *qyIs127[laminin::mCherry]*, *qyIs161[emb-9::Dendra]*, *qyIs87[vab-19::GFP]*, *qyIs89[vab-19::GFP]*, *qyIs108[laminin::Dendra]*, *qyIs109[laminin::Dendra]*, *qyIs43[pat-3::GFP; genomic ina-1]*; **LGI** (linkage group I), *ayIs4[egl-17>GFP]*, *lrp-1(ku156)*, *gld-1(q266)*, *inx-13(ok236)*, *clec(tm1291)*, *dpy-5(e61)*; **LGIH**, *vab-19(e1036)*, *rff-3(pk1426)*, *qyIs23[cdh-3>mCherry::PLCδ^{PH}]*, *clr-1(e1745)*; **LGIHII**, *unc-119(ed4)*, *ina-1(gm39)*, *ten-1(ok641)*; **LGIIV**, *lin-3(n1059)*, *lin-3(n378)*, *let-653(s1733)*, *tag-144(ok750)*, *qyIs42[pat-3::GFP; genomic ina-1]*, *qyIs15[zmp-1>HA-β-tail]*, *qyIs10[laminin::GFP]*; **LGV**, *mig-6(ev700)*, *rde-1(ne219)*, *qyIs44[emb-9::mCherry]*, *wsp-1(gm324)*; **LGX**, *cht1-1(ok1695)*, *him-4(rh319)*, *osm-11(n1604)*, *qyIs24[cdh-3>mCherry::PLCδ^{PH}]*, *qyIs7[laminin::GFP]*, *qyIs10[laminin::GFP]*, *qyIs46[emb-9::mCherry]*. See Supplementary Tables S4 and S5 for all new transgenic strains and primer sequences for generation of new PCR fusion constructs.

Microscopy, image acquisition, processing and analysis. Images were acquired using a Yokogawa spinning disc confocal scan head mounted on a Zeiss AxioImager microscope with a ×100 Plan-APOCHROMAT objective controlled by iVision software (Biovision Technologies) or using a Zeiss AxioImager microscope with a ×100 Plan-APOCHROMAT objective equipped with a Zeiss AxioCam MRm CCD camera controlled by Axiovision software (Zeiss Microimaging). Acquired images were processed using Photoshop CS3 Extended (Adobe Systems). Three-dimensional reconstructions were built from confocal z-stacks, analysed and exported as .mov files using IMARIS 6.0 (Bitplane). Spectral representations of the fluorescent intensities of VAB-19::GFP and PAT-3::GFP expression (two independent lines each) were constructed using Image J 1.40 g software.

Uterine–vulval tissue separation. To examine the relationship between the gonadal and ventral epidermal basement membranes (which are normally tightly juxtaposed and cannot be resolved by light microscopy), we incubated worms for one hour in M9 medium, under a coverslip, on 5% agar pads containing 0.01 M NaN₃. Under these conditions, the uterine and vulval tissues can separate from each other, enabling their respective basement membranes to be individually examined.

Mosaic analysis of VAB-19::GFP and PAT-3::GFP expression. Because the uterine and vulval tissues are tightly juxtaposed, a mosaic expression analysis was conducted to determine the origin of the VAB-19 and INA-1/PAT-3 that localized at the basement membrane gap boundary. *qyEx36[pat-3::GFP; genomic ina-1]* and *qyEx76[vab-19::GFP]* lines were examined for somatic loss of the transgene in either the uterine or vulval lineage (determined by absence of fluorescence in the tissue), but the complementary presence in the vulval or uterine lineage, respectively.

Cell ablations. Laser-directed cell ablations of the anchor cell, ventral uterine cells, dorsal uterine cells and VPCs were carried out on 5% agar pads as previously described⁸. Ablated animals were recovered from the agar pad, left to develop at 20 °C and then examined for anchor cell invasion and boundary-position defects at indicated times.

RNA interference. Double-strand RNA (dsRNA) used in this study was delivered by feeding to *wsp-1(gm324)*, *qyIs23[cdh-3>mCherry::PLCδ^{PH}]*, *qyIs10[laminin::GFP]*, *rff-3(pk1426)*, uterine-*(fos-1a>rde-1)* and VPC-specific *(unc-62>rde-1)* RNAi-sensitive strains. VPC- and uterine-specific RNAi was conducted by expression of RDE-1 under the control of the vulval-specific *unc-62* promoter¹³ and the uterine-specific *fos-1a* promoter as described³³. The tissue specificity of both was confirmed with RNAi targeting genes that have known specific functions in the uterine (*pat-3*, *fos-1a*) and vulval (*lin-39*) tissues. All RNAi vectors were from the Vidal or Ahinger libraries^{32,33} and sequenced to verify the correct insert.

Quantifying the breach in the basement membrane. The diameter of the breach in the basement membrane was measured at five developmental stages: P6.p four-, late four-, six-, early eight- and eight-cell stages. The position of the basement membrane breach was scored either by observation of the phase-dense line under DIC optics or by laminin::GFP. In all cases an unpaired Student *t*-test was used to determine the statistical significance of observed differences between stages. The anterior and posterior boundaries of the breach were scored independently at the early L4 and mid-L4 larval stages (see Table 1).

Optical highlighting (photoconversion) of basement membrane components. Dendra DNA sequence³⁶ was engineered to contain *C. elegans* codon usage⁵⁴ and three synthetic introns (the sequence is available on request). Dendra fusion constructs were made by inserting the *C. elegans* modified Dendra into the *mluI* site of pGK39 (*laminin::GFP*) and the *MscI* and *BsrGI* sites of pJK750 (*type IV collagen::mCherry*). Constructs were injected and integrated strains made as described previously²¹. Transgenic worms were photoconverted using a Zeiss LSM 510 confocal microscope (Zeiss Microimaging), equipped with a ×63 objective, scanning regions of interest with a 405 nm laser at 1 mW power for 30 s. After photoconversion, images were captured using a spinning disc confocal microscope or a Zeiss AxioImager. Animals were recovered from the agar pad, left to develop at 20 °C for the specified amount of time and then reimaged. Identical settings were used to acquire images at all times. The sum fluorescence intensity of photoconverted Dendra was quantified using Image J 1.40 g software and a seven-pixel-wide linescan. For more details on photoconversion of basement membrane methods used in this study see Nature Protocols⁵⁵.

Volumetric measurements of uterine and vulval tissues. Three-dimensional isosurface renderings were generated from confocal z-stacks of vulval- or uterine-specific GFP expression (*unc-62>GFP* and *fos-1>GFP* strains, respectively), using Imaris 7.1.1 (Bitplane). A fluorescence intensity threshold was set so isosurfaces were built in place of the uterine or vulval tissue. The volume of isosurfaces was used to estimate the volume of the respective tissue at the four- and eight-cell stage (*n* ≥ 8 for each).

51. Brenner, S. The genetics of *Caenorhabditis elegans*. *Genetics* **77**, 71–94 (1974).
52. Fraser, A. G. *et al.* Functional genomic analysis of *C. elegans* chromosome I by systematic RNA interference. *Nature* **408**, 325–330 (2000).
53. Rual, J. F. *et al.* Toward improving *Caenorhabditis elegans* phenotype mapping with an ORFeome-based RNAi library. *Genome Res.* **14**, 2162–2168 (2004).
54. Green, R. A. *et al.* Expression and imaging of fluorescent proteins in the *C. elegans* gonad and early embryo. *Methods Cell Biol.* **85**, 179–218 (2008).
55. Hagedorn, E. & Sherwood, D. Optically highlighting basement membrane components *C. elegans*. *Protocol Exchange* doi:10.1038/protex.2011.230 (2011).

DOI: 10.1038/ncb2233

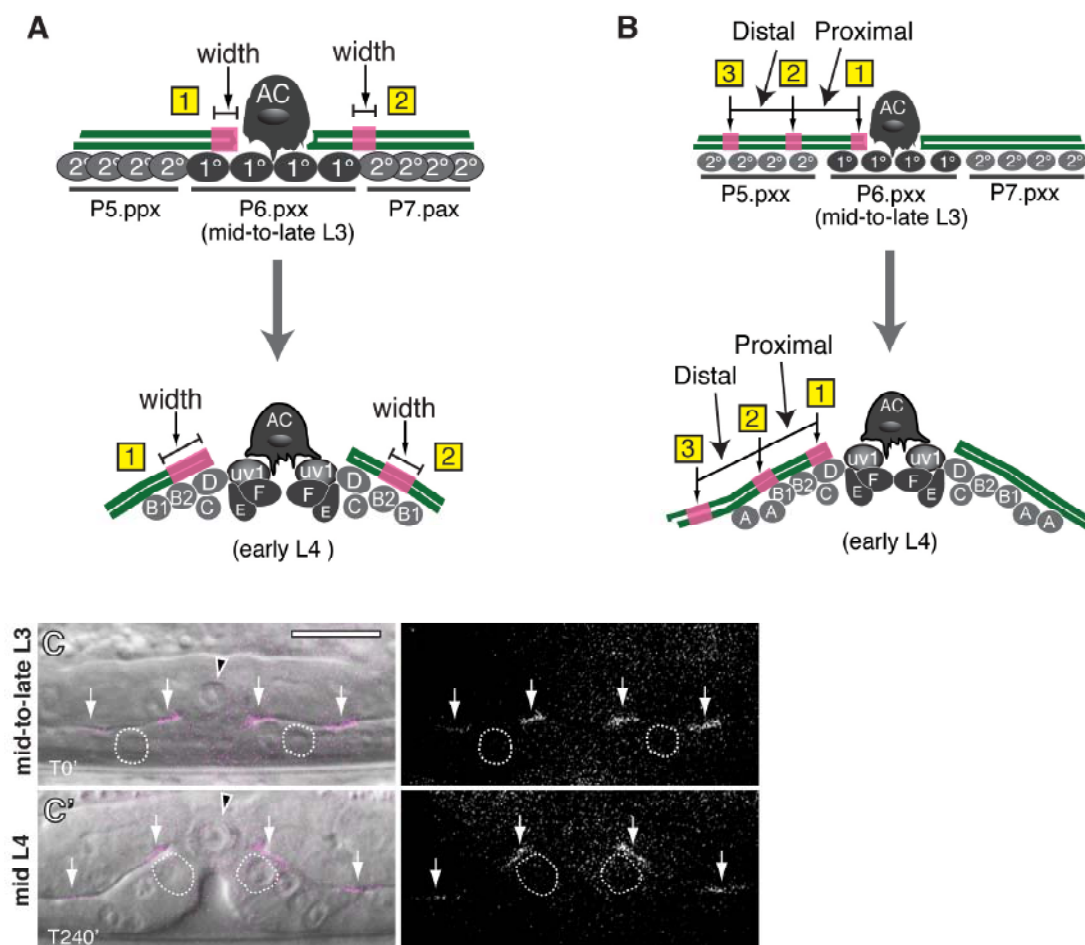


Figure S1 Optical Highlighting BM during Gap Enlargement. Anterior is left and ventral is down; black arrowheads indicate the AC in this and all other supplemental figures. (A and B) Schematic diagrams depict experimental designs of BM optical highlighting experiments (Figure 4). (A) Two regions of BM, one at the BM gap boundary (1) and one at a distance from the gap (2), were photoconverted at the mid-to-late L3 stage (top) and then examined later at the early L4 stage (bottom). The ratio of the width of the regions at the L4 stage to the width of the regions at the mid-to-late L3 stage was used to determine if the BM at the gap boundary had compressed or expanded over time or changed in fluorescence intensity (quantification is shown in Figure 4C and 4D). (B) Three regions of BM were photoconverted (1-3) at the mid-to-late L3 stage (top) and then reimaged at the early L4 stage (bottom). The

ratio of the distance between the regions (between 1 and 2, proximal; between 2 and 3, distal) at the early L4 stage to the distance between the regions at the mid-to-late L3 stage was used to determine whether the BM nearest to the boundary of the breach compressed or expanded over time (quantification is shown in Figure 4E). (C) DIC image of a mid-to-late L3 stage animal overlaid with photoconverted type IV collagen::Dendra (magenta, left) and corresponding grayscale of fluorescence (right). White dotted lines depict vulD cell positions. (C') Same animal as C, 240 minutes later, where the regions of photoconverted type IV collagen::Dendra at the gap boundary have moved during BM gap expansion from a location over the vulF precursor cell to a position over the vulD cell (white arrows, $n = 12/12$ animals examined). Scale bar represents 10 μm in this and all subsequent supplemental figures.

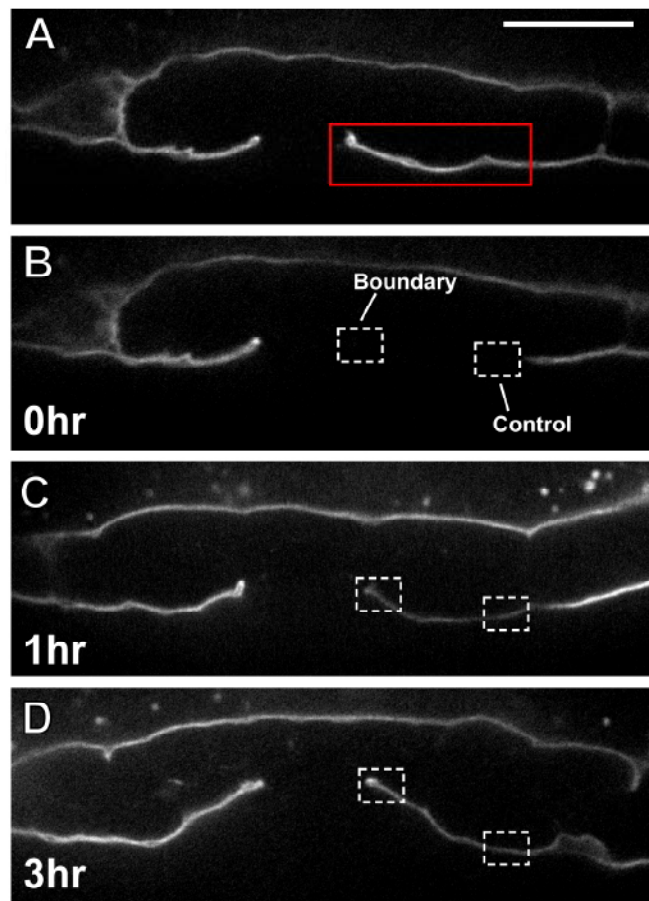


Figure S2 Basement Membrane Deposition is not Reduced at the Expanding BM Gap Boundary. (A-D) Grayscale images show laminin::GFP fluorescence over the course of BM gap expansion during a photobleaching recovery experiment. Images show animal prior to photobleaching (red box; A), immediately after photobleaching (B), and at time points one hour (C) and three hours (D) after photobleaching. As the gap in the BM expanded, the

mean fluorescence intensity of the BM was measured at two places: (1) at the boundary of the expanding hole in the BM and (2) at a distance from the hole (control). The fluorescent recovery of the two regions was compared to elucidate differences in the rate of BM deposition at the boundary of the expanding gap. BM deposition was not reduced at the boundary compared to the control regions ($n = 13/13$).

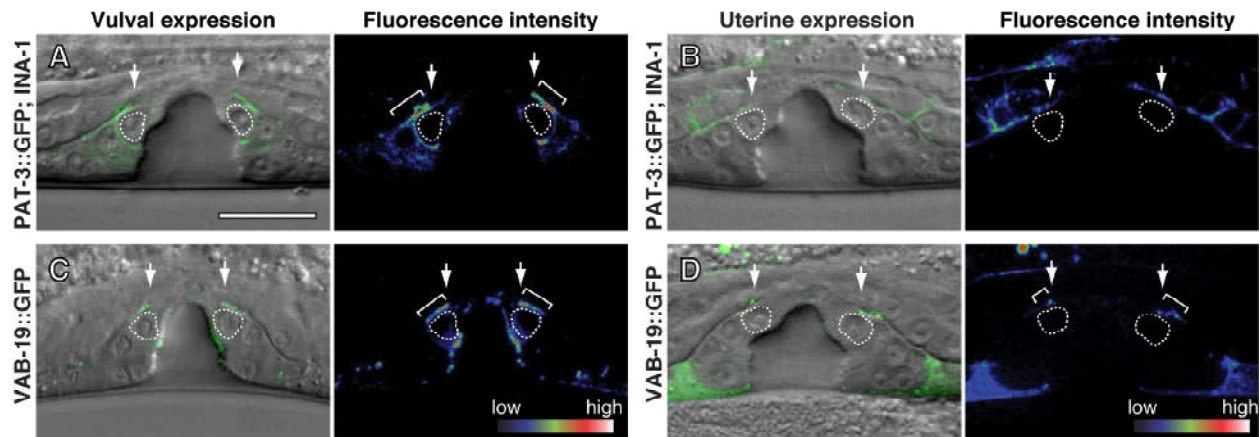


Figure S3 PAT-3::GFP (Integrin) and VAB-19::GFP (Kank) Localization at the BM Gap Boundary. (A-D) Mosaic analysis with *vab-19::GFP* and *pat-3::GFP* extrachromosomal (Ex) lines. DIC image overlaid with GFP fluorescence (green; left) and spectral representation of fluorescence intensity (right). (A and C) Images show mosaic animals where *pat-3::GFP* and *vab-19::GFP* extrachromosomal arrays were lost in the uterine cells, but maintained in vulval cells. PAT-3::GFP and VAB-19::GFP were expressed at high levels in the vulD cells (inverted brackets) and localized to the basal membrane

in contact with BM at the BM gap boundary (white arrows, $n = 30$ animals observed for each). (B and D) Images show mosaic animals where *pat-3::GFP* and *vab-19::GFP* extrachromosomal arrays were lost in the vulval cells, but maintained in uterine cells. PAT-3::GFP was expressed at low levels within uterine cells but was not concentrated at the BM gap boundary (white arrows). VAB-19::GFP was expressed at low levels in uterine cells (brackets) and polarized at the BM gap boundary ($n = 30$ animals observed for each).

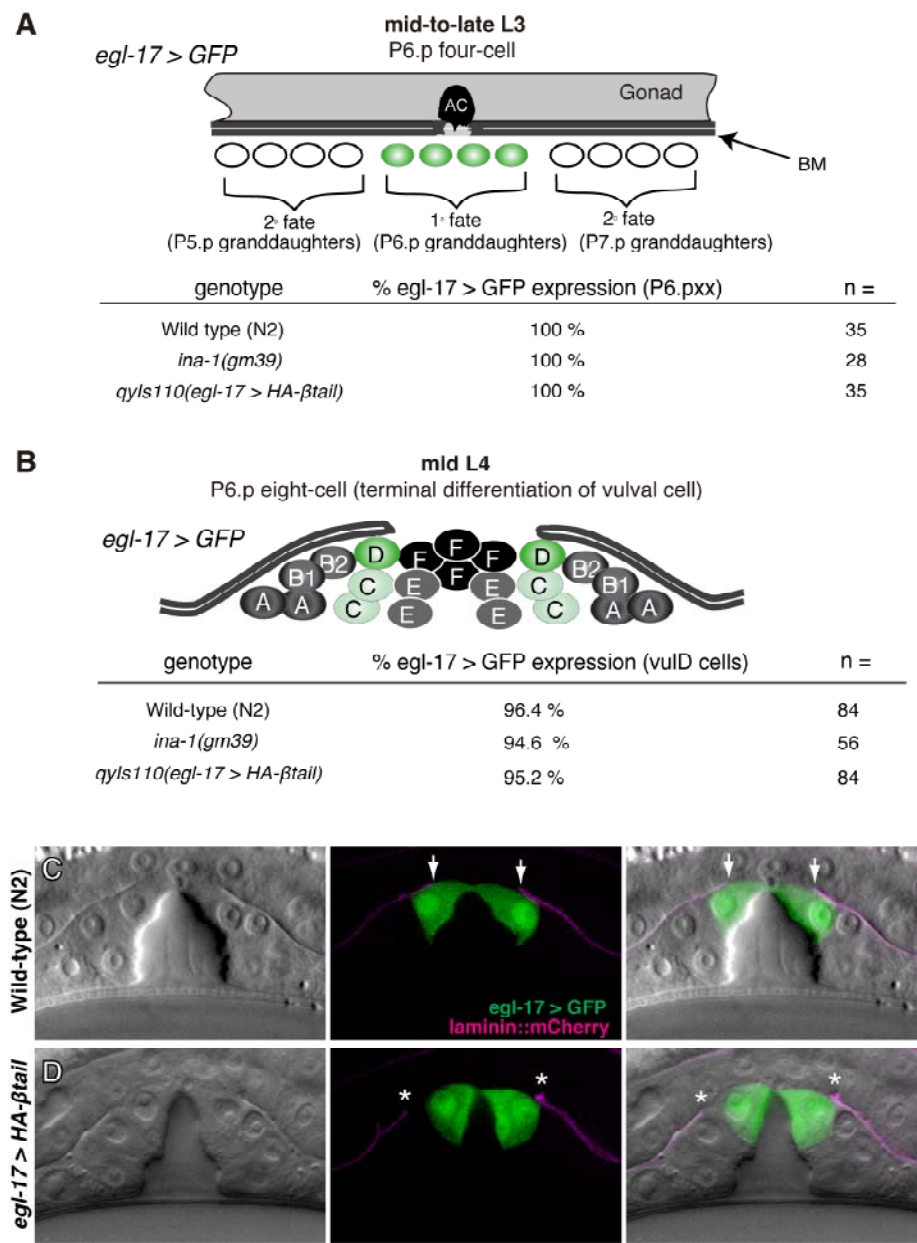


Figure S4 The VPCs are Properly Specified after Loss of Integrin Function. (A and B) Schematic diagrams depict dynamic wild-type expression pattern of *egl-17* > GFP (green), a marker for 1° and 2° vulval fate specification. (A) During the mid-to-late L3 larval stage *egl-17* > GFP is expressed in the 1° fated P6.p granddaughters. (B) During the late L3 stage *egl-17* > GFP expression is turned off in the 1° P6.p cell descendants and is turned on in the 2° fated vulC and vulD cells. Tables report the percentage of animals that properly express *egl-17* > GFP at

the mid-to-late L3 stage (A) and at the mid L4 stage (B). (C-D) DIC image (left), *egl-17* > GFP expression (green) and laminin::mCherry (magenta) fluorescence (middle) and DIC overlaid with fluorescence (right). (C) White arrows point to normal boundary positions in a wild-type animal with *egl-17* > GFP strongly expressed in the vulD cells. (D) In *qyls110(egl-17 > HA-βtail)* animals the boundary of the breach in the BM expands beyond the vulD cells at the mid L4 larval stage (asterisks), but *egl-17* > GFP expression is normal.

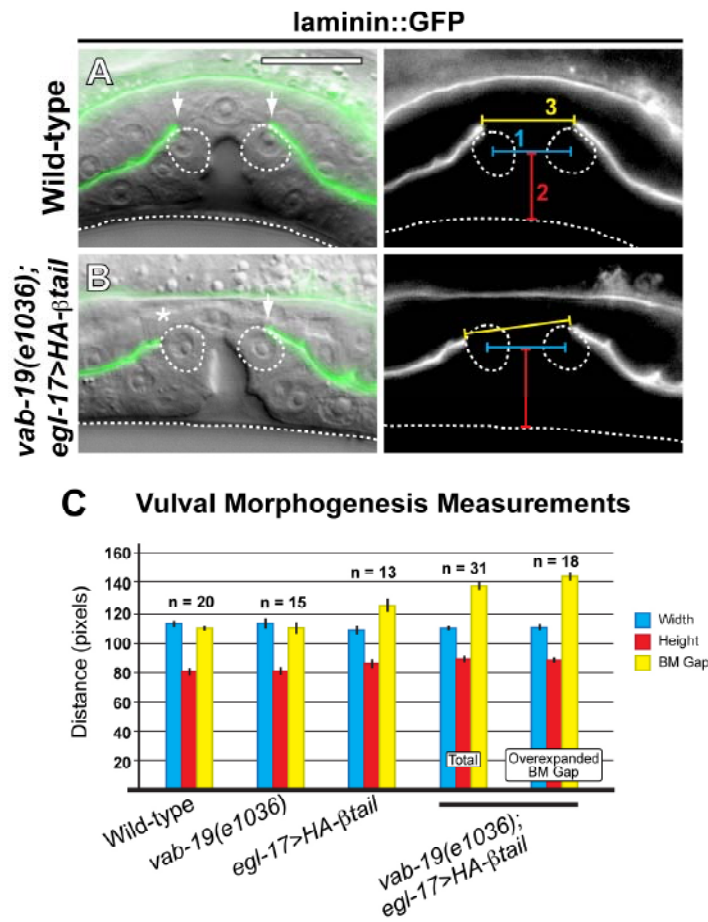


Figure S5 Vulval Morphogenesis is Normal When BM Gap Hyper-expands. (A-B) DIC image overlaid with laminin::GFP fluorescence (green, left); grayscale of laminin::GFP fluorescence with measurements of vulval morphogenesis depicted (right). White dotted lines denote vulD cell positions and the ventral surface of the animals; arrows point to boundary of BM gap. (A) Images show wild-type animal at the mid L4 stage. (B) Images show *vab-19(e1036); egl-17 > HA-βtail* animal where the BM gap has over-expanded (asterisk). (C)

Bar graph shows measurements of vulval morphogenesis in wild-type and different mutant or transgenic backgrounds. The width between the vulD cells (measurement 1 in A-B; blue), the height of the vulval invagination (measurement 2; red), and the width of the BM gap (measurement 3; yellow) were measured for each genetic background. The width and height of vulval invagination was not significantly different than wild-type in all cases examined (Student's t-test). Error bars report the standard error of the mean.

Supplementary Movie Legends

Movie S1 Prior to AC invasion an Intact BM Separates the Uterine and Vulval Tissues. Anterior is left and ventral is down in this and all other supplemental movies. The AC is expressing the plasma membrane marker *cdh-3 > mCherry::PLCδ^{PH}* (magenta) and the BM is visualized with laminin::GFP (green). Prior to AC invasion a 3D reconstruction reveals an intact BM separating the uterine and vulval tissues of a wild-type animal at the P6.p two-cell stage (movie corresponds to animal shown in Figure 1B). Scale bar represents 10 μm in this and all other supplemental movies.

Movie S2 During AC Invasion the AC is in Contact with the Gap in the BM. At the P6.p four-cell stage, the AC has invaded and generated in gap in the BMs separating the uterine and vulval tissues. At this time the AC is in continuous contact with the boundary of the gap in the BM. The animal in this movie is the same animal shown Figure 1C.

Movie S3 After AC Invasion, the Breach in the BM Expands Beyond the AC. By the late P6.p four-cell stage, the boundary of the gap in the BM expands beyond the AC. Sites of lost contact between the AC and the boundary of the hole in the BM are visible. The animal in this movie corresponds to the animal shown in Figure 1D.

Movie S4 The Breach in the BM Expands Beyond the AC at the early L4. At the early P6.p eight-cell stage (early L4 larval stage), the breach in the BM has expanded beyond the width of the AC. By this time, the AC no longer contacts the boundary of the gap in the BM. The animal in this movie is the same animal shown in Figure 1E.

Movie S5 In Vulvaless Animals the Breach in the BM Fails to Expand. Movie shows spatial relationship of the BM (visualized with laminin::GFP, green) and the AC (expressing *cdh-3 > mCherry::PLCδ^{PH}*, magenta) When the AC invades in *lin-3 (n1059/n378)* mutants (which are Vulvaless), the breach in the BM never expands beyond the width of the AC. The animal in this movie is the same animal shown in Figure 3B.

II. Supplemental Tables

Table S1. Genes with Signal Peptide Processing or Peptidase Processing Gene Ontology Annotation Screened for Pvl Phenotype.

Sequence Name (Gene) ^a	Gene Public Name	KOG Info (merged)
4R79.1	nas-6	[KOG3714] Meprin A metalloprotease
AC3.5	AC3.5	[KOG1046] Puromycin-sensitive aminopeptidase and related aminopeptidases
B0218.8	clec-52	[KOG4297] C-type lectin
B0222.5*	B0222.5	[KOG4295] Serine proteinase inhibitor (KU family)
B0238.12	B0238.12	[LSE0566] Uncharacterized protein
B0238.7	B0238.7	[KOG1516] Carboxylesterase and related proteins
B0286.6*	try-9	[KOG3627] Trypsin
B0495.7	B0495.7	[KOG2194] Aminopeptidases of the M20 family
C02B4.1	adt-1	[KOG3538] Disintegrin metalloproteinases with thrombospondin repeats
C02f12.5*	C02F12.5	
C02G6.1*	C02G6.1	[KOG0959] N-arginine dibasic convertase NRD1 and related Zn ²⁺ -dependent endopeptidases, insulinase superfamily
C02G6.2	C02G6.2	[KOG0959] N-arginine dibasic convertase NRD1 and related Zn ²⁺ -dependent endopeptidases, insulinase superfamily
C03G6.18	srp-5	
C03G6.19	srp-6	[KOG2392] Serpin
C04A11.4	adm-2	[KOG3607] Meltrins, fertilins and related Zn-dependent metalloproteinases of the ADAMs family
C04F12.10	fce-1	[KOG2719] Metalloprotease
C05D11.6	nas-4	[KOG3714] Meprin A metalloprotease
C05E4.1	srp-2	[KOG2392] Serpin
C05E4.3	srp-1	[KOG2392] Serpin
C07D10.4	nas-7	[KOG3714] Meprin A metalloprotease
C07G1.1	try-2	[KOG3627] Trypsin
C08H9.1	C08H9.1	[KOG1282] Serine carboxypeptidases (lysosomal cathepsin A)
C10C5.3	C10C5.3	[KOG2275] Aminoacylase ACY1 and related metalloexopeptidases
C10C5.4	C10C5.4	[KOG2275] Aminoacylase ACY1 and related metalloexopeptidases
C10C5.5	C10C5.5	[KOG2275] Aminoacylase ACY1 and related metalloexopeptidases
C10G8.2	C10G8.2	[KOG4295] Serine proteinase inhibitor (KU family)
C10G8.3	C10G8.3	[KOG4295] Serine proteinase inhibitor (KU family)
C10G8.4	C10G8.4	[LSE0566] Uncharacterized protein
C11D2.2*	C11D2.2	
C15C8.3	C15C8.3	[KOG1339] Aspartyl protease
C17G1.6	nas-37	[KOG3714] Meprin A metalloprotease
C24F3.3	nas-12	[KOG3714] Meprin A metalloprotease
C25B8.3	cpr-6	[KOG1543] Cysteine proteinase Cathepsin L
C25E10.8	C25E10.8	[LSE0566] Uncharacterized protein
C26B9.5	C26B9.5	[KOG2182] Hydrolytic enzymes of the alpha/beta hydrolase fold
C26C6.3	nas-36	
C27C12.7	dpf-2	[KOG2100] Dipeptidyl aminopeptidase
C28F5.4	C28F5.4	
C31B8.8	C31B8.8	[KOG1565] Gelatinase A and related matrix metalloproteases
C32B5.13	C32B5.13	[KOG1543] Cysteine proteinase Cathepsin L
C32B5.7	C32B5.7	

C33F10.7	lact-5	[LSE0720] Predicted esterase
C34D4.9*	nas-8	[KOG3714] Meprin A metalloprotease
C34F6.1	C34F6.1	[KOG4295] Serine proteinase inhibitor (KU family)
C34H3.1	tag-275	[KOG3607] Meltrins, fertilins and related Zn-dependent metalloproteinases of the ADAMs family
C35C5.2	C35C5.2	
C36B1.12	imp-1	[KOG2442] Uncharacterized conserved protein, contains PA domain
C37C3.6	mig-6	[KOG4597] Serine proteinase inhibitor (KU family) with thrombospondin repeats
C37H5.9	nas-9	[KOG3714] Meprin A metalloprotease
C42C1.11*	C42C1.11	[KOG1047] Bifunctional leukotriene A4 hydrolase/aminopeptidase LTA4H
C43G2.5	try-3	[KOG3627] Trypsin
C44B7.11	C44B7.11	
C44E12.1	C44E12.1	[KOG2275] Aminoacylase ACY1 and related metalloexopeptidases
C47E12.8	dhp-2	[KOG2584] Dihydroorotase and related enzymes
C49D10.10	C49D10.10	[KOG3624] M13 family peptidase
C50F4.3	tag-329	[KOG1543] Cysteine proteinase Cathepsin L
C50H2.3	mec-9	[KOG4295] Serine proteinase inhibitor (KU family)
C51E3.7	egl-3	[KOG3526] Subtilisin-like proprotein convertase
C52E4.1	cpr-1	[KOG1543] Cysteine proteinase Cathepsin L
C53B7.2	C53B7.2	
C53B7.7	C53B7.7	[KOG3624] M13 family peptidase
C54D1.2	clec-86	[KOG4297] C-type lectin
C54D10.10	C54D10.10	
C54E4.2	C54E4.2	[KOG3555] Ca ²⁺ -binding proteoglycan Testican
DY3.7	sup-17	[KOG3658] Tumor necrosis factor-alpha-converting enzyme (TACE/ADAM17) and related metalloproteases
E01G6.1	E01G6.1	
EEED8.6	EEED8.6	
EGAP1.3	zmp-1	
F01D4.4	egl-21	[KOG2649] Zinc carboxypeptidase
F01F1.5	dpf-4	[KOG2100] Dipeptidyl aminopeptidase
F01F1.9	F01F1.9	[KOG2596] Aminopeptidase I zinc metalloprotease (M18)
F02D8.4	F02D8.4	
F02E9.9*	F02E9.9	
F08C6.1	adt-2	[KOG3538] Disintegrin metalloproteinases with thrombospondin repeats
F09C6.4	srp-10	
F09C6.5	srp-9	
F09E8.6	nas-14	[KOG3714] Meprin A metalloprotease
F10E7.4	spon-1	[KOG3539] Spondins, extracellular matrix proteins
F11A6.1	kpc-1	[KOG3525] Subtilisin-like proprotein convertase
F12A10.4	F12A10.4	[KOG3624] M13 family peptidase
F13D12.6	F13D12.6	[KOG1282] Serine carboxypeptidases (lysosomal cathepsin A)
F13H6.3	F13H6.3	[KOG1516] Carboxylesterase and related proteins
F15D4.4	F15D4.4	[KOG1543] Cysteine proteinase Cathepsin L
F16F9.4	F16F9.4	[KOG1515] Arylacetamide deacetylase
F18A12.1	F18A12.1	[KOG3624] M13 family peptidase
F18A12.4	F18A12.4	[KOG3624] M13 family peptidase
F18A12.5	F18A12.5	[KOG3624] M13 family peptidase
F18A12.6*	F18A12.6	
F18A12.8	F18A12.8	[KOG3624] M13 family peptidase

F20D6.3	srp-8	[KOG2392] Serpin
F20D6.4	srp-7	[KOG2392] Serpin
F20G2.4	nas-24	[KOG3714] Meprin A metalloprotease
F21F8.2	F21F8.2	[KOG1339] Aspartyl protease
F21F8.3	asp-5	[KOG1339] Aspartyl protease
F21F8.4	F21F8.4	[KOG1339] Aspartyl protease
F21F8.7	asp-6	[KOG1339] Aspartyl protease
F21H12.6*	F21H12.6	[KOG1114] Tripeptidyl peptidase II
F23B2.11	pcp-3	
F23B2.12	pcp-2	[KOG2182] Hydrolytic enzymes of the alpha/beta hydrolase fold
F25E5.10	try-8	[KOG3627] Trypsin
F25E5.3	F25E5.3	[KOG3627] Trypsin
F25E5.4	F25E5.4	[KOG3627] Trypsin
F25E5.7	F25E5.7	[KOG3627] Trypsin
F25H8.3	gon-1	
F26E4.3	F26E4.3	
F26G1.6	F26G1.6	[KOG3624] M13 family peptidase
F28A12.4	F28A12.4	[KOG1339] Aspartyl protease
F29G6.1	F29G6.1	
F30H5.3*	F30H5.3	[KOG4295] Serine proteinase inhibitor (KU family)
F32A5.3	F32A5.3	[KOG1282] Serine carboxypeptidases (lysosomal cathepsin A)
F32A7.6	aex-5	[KOG3525] Subtilisin-like proprotein convertase
F32B5.8	cpz-1	[KOG1543] Cysteine proteinase Cathepsin L
F32D8.3	F32D8.3	
F32H5.1	F32H5.1	[KOG1543] Cysteine proteinase Cathepsin L
F35B12.4	F35B12.4	[KOG4295] Serine proteinase inhibitor (KU family)
F35B12.6	tag-290	[KOG4295] Serine proteinase inhibitor (KU family)
F35H12.3	sel-12	[KOG2736] Presenilin
F36D3.9*	cpr-2	
F38E9.2	nas-39	
F39D8.4	nas-13	[KOG3714] Meprin A metalloprotease
F39E9.4	F39E9.4	[KOG3624] M13 family peptidase
F39E9.6	F39E9.6	[KOG3624] M13 family peptidase
F40A3.3	F40A3.3	[KOG3346] Phosphatidylethanolamine binding protein
F40E10.1	hch-1	[KOG3714] Meprin A metalloprotease
F41C3.5	F41C3.5	[KOG1282] Serine carboxypeptidases (lysosomal cathepsin A)
F41G3.12	agr-1	
F42A10.8	nas-28	
F44B9.1	dpf-6	[KOG2100] Dipeptidyl aminopeptidase
F44C4.3*	cpr-4	[KOG1543] Cysteine proteinase Cathepsin L
F45G2.1	nas-1	[KOG3714] Meprin A metalloprotease
F46B3.5	grd-2	[KOG3638] Sonic hedgehog and related proteins [LSE3909] Unnamed protein
F46C5.3	nas-25	[KOG3714] Meprin A metalloprotease
F48A9.3	try-6	
F49E8.3	pam-1	[KOG1046] Puromycin-sensitive aminopeptidase and related aminopeptidases
F53B6.5	F53B6.5	[KOG2775] Metallopeptidase
F54F11.2	F54F11.2	[KOG3624] M13 family peptidase
F55D10.3	F54F11.2	
F56A4.1*	glit-1	[KOG1516] Carboxylesterase and related proteins

F56D2.1	nas-2	
F56F10.1*	ucr-1	[KOG0960] Mitochondrial processing peptidase, beta subunit, and related enzymes (insulinase superfamily)
F57B7.4	F56F10.1	[KOG2182] Hydrolytic enzymes of the alpha/beta hydrolase fold
F57C12.1	mig-17	[KOG3538] Disintegrin metalloproteinases with thrombospondin repeats
F57F5.1	nas-38	[KOG3714] Meprin A metalloprotease
F58A6.4	F57F5.1	
F58B4.1	nas-29	
F59A3.1	nas-31	
F59D6.2	F59A3.1	[KOG2649] Zinc carboxypeptidase, [KOG3714] Meprin A metalloprotease
F59D6.3	F59D6.2	[KOG1339] Aspartyl protease
H14N18.4	F59D6.3	[KOG1339] Aspartyl protease
H19M22.3	H14N18.4	
H22K11.1	H19M22.3	[KOG1565] Gelatinase A and related matrix metalloproteases
H27A22.1	asp-3	[KOG1339] Aspartyl protease
H36L18.1	H27A22.1	[KOG3946] Glutaminyl cyclase
K01G5.9	H36L18.1	
K02E7.10	K01G5.9	[KOG1592] Asparaginase
K02F2.1	K02E7.10	[KOG1543] Cysteine proteinase Cathepsin L
K02F6.9	dpf-3	[KOG2281] Dipeptidyl aminopeptidases/acylaminoacyl-peptidases
K03B8.1	K02F6.9	[KOG3624] M13 family peptidase
K03B8.2	nas-16	[KOG3714] Meprin A metalloprotease
K03B8.3	nas-17	[KOG3714] Meprin A metalloprotease
K03B8.5	nas-18	[KOG3714] Meprin A metalloprotease
K03D10.1	nas-19	[KOG3714] Meprin A metalloprotease
K04E7.3	kal-1	[KOG4802] Adhesion-type protein
K04F10.4	nas-33	
K06A4.1*	bli-4	[KOG3525] Subtilisin-like proprotein convertase
K07A1.6	nas-3	[KOG3714] Meprin A metalloprotease
K07C11.5	K07A1.6	[LSE0566] Uncharacterized protein
K08B4.6	cri-2	[KOG4745] Metalloproteinase inhibitor TIMP and related proteins
K09C8.3	cpi-1	[LSE3967] Unnamed protein
K10B2.2	nas-10	[KOG3714] Meprin A metalloprotease
K10C2.1*	K10B2.2	[KOG1282] Serine carboxypeptidases (lysosomal cathepsin A)
K10C2.3*	K10C2.1	[KOG1282] Serine carboxypeptidases (lysosomal cathepsin A)
K10D3.4	K10C2.3	[KOG1339] Aspartyl protease
K11D12.6	K10D3.4	[KOG4295] Serine proteinase inhibitor (KU family)
K11D12.7*	K11D12.6	[KOG4295] Serine proteinase inhibitor (KU family)
K11G12.1*	K11D12.7	[KOG4295] Serine proteinase inhibitor (KU family)
K12C11.1	nas-11	[KOG3714] Meprin A metalloprotease
K12H4.7	K12C11.1	[KOG2737] Putative metallopeptidase
M04C9.3	K12H4.7	[KOG2182] Hydrolytic enzymes of the alpha/beta hydrolase fold
M04G12.2	M04C9.3	[KOG4755] Predicted pyroglutamyl peptidase
M05D6.4	cpz-2	[KOG1543] Cysteine proteinase Cathepsin L
M28.6	lact-4	[LSE0720] Predicted esterase
R01B10.1	lact-3	[LSE0720] Predicted esterase
R03G8.4	cpi-2	[LSE3967] Unnamed protein
R03G8.6	R03G8.4	[KOG1046] Puromycin-sensitive aminopeptidase and related aminopeptidases
R04B3.2	R03G8.6	[KOG1046] Puromycin-sensitive aminopeptidase and related aminopeptidases
R07E3.1	R04B3.2	[KOG1593] Asparaginase

R09F10.1	R07E3.1	[KOG1542] Cysteine proteinase Cathepsin F
R11A5.7	R09F10.1	[KOG1542] Cysteine proteinase Cathepsin F
R11E3.7*	R11A5.7	[KOG2650] Zinc carboxypeptidase
R11E3.8	dpf-7	
R11H6.1	dpf-5	[KOG2100] Dipeptidyl aminopeptidase
R12A1.3	pes-9	[KOG2276] Metalloexopeptidases
R12H7.2	R12A1.3	
R15I.5	asp-4	[KOG1339] Aspartyl protease
T02B11.7	dpy-31	[KOG3714] Meprin A metalloprotease
T03D8.3	nas-32	[KOG3714] Meprin A metalloprotease
T03D8.6	sbt-1	[KOG4187] Proprotein convertase (PC) 2 chaperone involved in secretion (neuroendocrine protein 7B2)
T03E6.7	T03D8.6	[KOG2410] Gamma-glutamyltransferase
T03F1.10	cpl-1	[KOG1543] Cysteine proteinase Cathepsin L
T04F3.2	clec-53	
T04G9.2	T04F3.2	[KOG4578] Uncharacterized conserved protein, contains KAZAL and TY domains
T05A8.4	nas-15	
T05E11.5	nep-2	[KOG3624] M13 family peptidase
T05E11.6	imp-2	[KOG2443] Uncharacterized conserved protein
T05F1.1	T05E11.6	
T06A4.1	nra-2	[KOG2526] Predicted aminopeptidases - M20/M25/M40 family
T06D4.4*	T06A4.1	
T06E6.10	T06D4.4	[KOG3624] M13 family peptidase
T07F10.1	T06E6.10	[KOG1217] Fibrillins and related proteins containing Ca ²⁺ -binding EGF-like domains
T07H8.4	T07F10.1	[KOG1046] Puromycin-sensitive aminopeptidase and related aminopeptidases
T10B10.2	mec-1	[KOG4295] Serine proteinase inhibitor (KU family)
T10H4.12	ucr-2.2	[KOG2583] Ubiquinol cytochrome c reductase, subunit QCR2
T11F9.3	cpr-3	[KOG1543] Cysteine proteinase Cathepsin L
T11F9.5	nas-20	[KOG3714] Meprin A metalloprotease
T11F9.6*	nas-21	
T16A9.4	nas-22	
T18H9.2	T16A9.4	[KOG3624] M13 family peptidase
T19D2.1	asp-2	[KOG1339] Aspartyl protease
T21D11.1	T19D2.1	
T21D12.12	T21D11.1	[KOG1565] Gelatinase A and related matrix metalloproteases
T21D12.7	T21D12.12	[KOG4295] Serine proteinase inhibitor (KU family)
T22F7.3	T21D12.7	
T23F1.7	T22F7.3	
T23F4.4	dpf-1	[KOG2100] Dipeptidyl aminopeptidase
T23H4.3	nas-27	[KOG3714] Meprin A metalloprotease
T25B6.2	nas-5	[KOG3714] Meprin A metalloprotease
T27A8.1	T25B6.2	[KOG3624] M13 family peptidase
T27A8.3	T27A8.1	[KOG2649] Zinc carboxypeptidase
T28C12.4	T27A8.3	[KOG2775] Metallopeptidase
T28C12.5*	T28C12.4	[KOG1516] Carboxylesterase and related proteins
T28H10.3	T28C12.5	[KOG1516] Carboxylesterase and related proteins
W01A11.1	T28H10.3	[KOG1348] Asparaginyl peptidases
W01A8.6	W01A11.1	[KOG2565] Predicted hydrolases or acyltransferases (alpha/beta hydrolase superfamily)
W01F3.3	W01A8.6	

W03G9.4	mlt-11	
W05B2.2	app-1	[KOG2413] Xaa-Pro aminopeptidase
W07B8.1	W05B2.2	[KOG4295] Serine proteinase inhibitor (KU family)
W07B8.4	W07B8.1	[KOG1543] Cysteine proteinase Cathepsin L
W07B8.5*	W07B8.4	[KOG1543] Cysteine proteinase Cathepsin L
W08E12.7	cpr-5	[KOG1543] Cysteine proteinase Cathepsin L
W09B12.1	W08E12.7	[KOG2776] Metallopeptidase
W09D12.1	ace-1	[KOG4389] Acetylcholinesterase/Butyrylcholinesterase
Y113G7B.15	W09D12.1	[KOG1565] Gelatinase A and related matrix metalloproteases
Y116A8A.9	Y113G7B.15	
Y116A8C.4	map-2	[KOG2775] Metallopeptidase
Y116A8C.5	Y116A8C.4	
Y116F11B.3*	Y116A8C.5	
Y16B4A.2*	pcp-4	[KOG2182] Hydrolytic enzymes of the alpha/beta hydrolase fold
Y18H1A.9*	Y16B4A.2	
Y32G9A.4*	Y18H1A.9	[KOG2650] Zinc carboxypeptidase
Y37D8A.13	srp-3	[KOG2392] Serpin
Y37E11AL.7	unc-71	[KOG3607] Meltrins, fertilins and related Zn-dependent metalloproteinases of the ADAMs family
Y38H6C.8	map-1	[KOG2738] Putative methionine aminopeptidase
Y39A3B.1	Y38H6C.8	[KOG4297] C-type lectin
Y39B6A.20	Y39A3B.1	[KOG2194] Aminopeptidases of the M20 family
Y39B6A.21	asp-1	[KOG1339] Aspartyl protease
Y39B6A.22*	Y39B6A.21	
Y39B6A.23*	Y39B6A.22	[KOG1339] Aspartyl protease
Y39B6A.24*	Y39B6A.23	
Y40D12A.2	Y39B6A.24	[KOG1339] Aspartyl protease
Y40H7A.10	Y40D12A.2	[KOG1282] Serine carboxypeptidases (lysosomal cathepsin A)
Y43F4A.1	Y40H7A.10	[KOG1543] Cysteine proteinase Cathepsin L
Y43F8A.3	Y43F4A.1	[KOG2556] Leishmanolysin-like peptidase (Peptidase M8 family)
Y43F8B.3	Y43F8B.3	
Y47G6A.19	Y47G6A.19	[KOG2650] Zinc carboxypeptidase
Y48B6A.7	ace-4	[KOG4389] Acetylcholinesterase/Butyrylcholinesterase
Y49G5A.1	Y49G5A.1	[KOG4295] Serine proteinase inhibitor (KU family)
Y51A2D.1	Y51A2D.1	
Y51A2D.8*	Y51A2D.8	[KOG1543] Cysteine proteinase Cathepsin L
Y54E10BR.5	Y54E10BR.5	[KOG3342] Signal peptidase I
Y55F3AM.8	immp-2	[KOG1568] Mitochondrial inner membrane protease, subunit IMP2
Y56A3A.2	Y56A3A.2	[KOG2921] Intramembrane metalloprotease (sterol-regulatory element-binding protein (SREBP) protease)
Y59C2A.1	Y59C2A.1	[KOG2650] Zinc carboxypeptidase
Y65B4A.2*	Y65B4A.2	[KOG1543] Cysteine proteinase Cathepsin L
Y70C5C.1	Y70C5C.1	[KOG0959] N-arginine dibasic convertase NRD1 and related Zn ²⁺ -dependent endopeptidases, insulinase superfamily
Y71H2AM.13*	Y71H2AM.13	[KOG1516] Carboxylesterase and related proteins
Y7A9A.1	Y7A9A.1	[KOG2410] Gamma-glutamyltransferase
Y95B8A.1*	nas-30	[KOG3714] Meprin A metalloprotease
ZC376.2	ZC376.2	[KOG1516] Carboxylesterase and related proteins
ZC581.6	try-7	[KOG3627] Trypsin [LSE0572] Uncharacterized protein
ZC84.1	ZC84.1	
ZC84.6	ZC84.6	

ZK1037.10	wrt-7	[KOG3638] Sonic hedgehog and related proteins
ZK112.1	pcp-1	[KOG2183] Prolylcarboxypeptidase (angiotensinase C)
ZK1248.1	ZK1248.1	[KOG3624] M13 family peptidase
ZK1290.12	wrt-1	[KOG3638] Sonic hedgehog and related proteins
ZK154.7	adm-4	[KOG3658] Tumor necrosis factor-alpha-converting enzyme (TACE/ADAM17) and related metalloproteases
ZK20.6	nep-1	
ZK287.4	ZK287.4	
ZK353.6	lap-1	[KOG2597] Predicted aminopeptidase of the M17 family
ZK377.1	wrt-6	[KOG3638] Sonic hedgehog and related proteins
ZK384.3	ZK384.3	
ZK524.1	spe-4	[KOG2736] Presenilin
ZK550.3*	ZK550.3	[KOG2089] Metalloendopeptidase family - saccharolysin & thimet oligopeptidase
ZK678.5	wrt-4	[KOG3638] Sonic hedgehog and related proteins
ZK688.6	pcp-5	
ZK945.1	lact-2	[LSE0720] Predicted esterase, [KOG2183] Prolylcarboxypeptidase (angiotensinase C)
ZK970.1	ZK970.1	[KOG3624] M13 family peptidase

^a Sequence name, gene name and KOG data are from wormbase 215 via www.ensembl.org.

* Denotes genes for which RNAi clone was unavailable.

Table S2. BM Boundary Position after RNAi mediated Knockdown of Selected Proteases.

Sequence Name (gene)	Gap Expansion ^a		
	Normal Boundary ^b	Overexpanded	Underexpanded
L4440 ^c	20	0	0
C10G8.4	20	0	0
C25E10.8	19	1	0
C27C12.7 (dpf-2)	20	0	0
C34H3.1 (tag-275)	19	0	1
F23B2.12 (pcp-2)	20	0	0
K03B8.3 (nas-18)	20	0	0
K10D3.4	20	0	0
T03D8.6 (sbt-1)	19	0	1
T27A8.1	19	1	0
Y40D12A.2	19	1	0

^a Genes in the *C. elegans* genome with either a peptidase processing or signal peptide processing gene ontology annotation were identified (Table S1). Feeding RNAi was used to target 87% of these genes for knockdown in *wsp-1(gm324)* mutants, a background sensitized for defects in uterine-vulval attachment. Genes whose knockdown resulted in a dramatic Pvl phenotype, indicative of a defect in uterine-vulval attachment, were then further scored for defects in BM boundary positioning in animals expressing laminin::GFP and the anchor cell marker, *cdh-3* > mCherry::PLCδ^{PH}. The genes *gon-1* and *ppn-1* were excluded from our analysis because RNAi mediated knockdown resulted in severe gonad defects that precluded scoring.

^b Scored as number of animals with BM boundary in contact with vulD between early and mid L4 (Figure 1).

^c Empty RNAi vector.

Table S3. BM Gap Position in Mutants of Secreted and Transmembrane Proteins with Roles in Uterine-vulval Attachment.

Genotype (Encoded product)	P6.p early 8-cell stage (early L4 stage)		Invasion at P6.p 4-cell stage
	% Expanded Gap Boundary ^a	n=	
Wild-type (N2)	0.0	100	25/25
<u>Transmembrane Proteins</u>			
<i>lrp-1(ku156)/gld-1(q266)/</i> (low-density lipoprotein (LDL) receptor-like protein)	1.7	60	25/25
<i>chtl-1(ok1695)/</i> (Choline transporter-like protein)	1.4	70	22/22
<i>tag-144(ok750)/nT-1/</i> (a KAP family P-loop predicted NTPase, with two or four transmembrane helices inserted into the P-loop NTPase domain)	0.0	60	24/24
<i>F41E7.1 (RNAi)/</i> (Na ⁺ /H ⁺ antiporter)	0.0	80	20/20
<i>ina-1(gm39)/</i> (integrin α subunit)	6.0	100	17/40
<i>clr-1(e1745)/</i> (a receptor tyrosine phosphatase)	0.0	60	25/25
<i>inx-13(ok236)/szT1</i> (innexin, an integral transmembrane channel protein)	L1 arrest		ND
<u>ECM Components and Secreted Proteins</u>			
<i>let-653(s1733/nT1)/</i> (mucin-like protein)	L1 arrest		ND
<i>mig-6(ev700)/</i> (papilin)	1.7	60	23/25
<i>him-4(rh319)/</i> (hemicentin)	2.5	80	25/30
<i>osm-11(n1604)/</i> (osm-11)	1.2	82	24/24
<i>cllec-1(tm1291)/</i> (C-type lectin)	0.0	80	24/24
<i>gon-1(e1254/nT-1)/</i> (metalloprotease with thrombospondin type 1 repeats)	ND ^b		14/14
<i>dpy-5(e61)/</i> (Group I cuticle procollagen)	0.0	60	20/20
<i>ten-1(ok641)/mT1/</i> (teneurin)	1.7	60	30/32

^a Gap expansion was scored by position of anterior and posterior boundaries in relation to the vulD cell under DIC optics. The BM boundary in wild-type animals is located over the vulD cell at the P6.p early eight-cell. Expanded gaps in the BM boundary were scored as extending beyond the vulD cell.

^b Severe gonad defects precluded scoring.

Table S4. Extrachromosomal Array and Strain Generation.

PCR Fusions				
Ex Designation	Is Designation	PCR Fusion Created	Injected Concentration	Co-injection Marker(s)
<i>qyEx138</i>	<i>qyIs138</i> , <i>qyIs139</i>	<i>unc-62 > RDE-1</i>	10 ng/μl	<i>unc-119+</i> <i>myo-2 > YFP</i>
<i>qyEx84</i>	<i>qyIs110</i> , <i>qyIs111</i>	<i>egl-17 > HA-βtail</i>	5 ng/μl	<i>unc-119+</i> <i>myo-2 > YFP</i>
Expression Vectors				
Ex Designation	Is Designation	Expression Gene	Injected Concentration	Co-injection Marker
<i>qyEx76</i>	<i>qyIs87</i> , <i>qyIs89</i>	<i>vab-19::GFP</i>	40 ng/μl	<i>unc-119+</i>
<i>N/A</i>	<i>qyIs127</i>	<i>lam-1::mCherry</i>	15 ng/μl	<i>unc-119+</i>
<i>qyEx37</i>	<i>qyIs46</i>	<i>emb-9::mCherry</i>	15 ng/μl	<i>unc-119+</i>
<i>qyEx91</i>	<i>qyIs108</i> , <i>qyIs109</i>	<i>lam-1::Dendra</i>	15 ng/μl	<i>unc-119+</i>
<i>qyEx185</i>	<i>qyIs161</i>	<i>emb-9::Dendra</i>	5 ng/μl	<i>unc-119+</i>

Table S5. Primer Sequences and Templates Used for PCR Fusions.

Primer Sequence	Primer Type	Amplicon	Template
5'ATGTAGCTGCCAGCCATGGATA3'	forward	<i>unc-62</i> > promoter	Fosmid WRM0629aH06
5'CAAAAAGTCATATATCATGACAG3'	forward nested	<i>unc-62</i> > promoter	Fosmid WRM0629aH06
5'GTTCTGCAAGAGAGAAATATTAA3'	reverse	<i>unc-62</i> > promoter	Fosmid WRM0629aH06
5'TAATGTGAGTTAGCTCACTCATTAGG3'	forward	<i>egl-17</i> > promoter	<i>egl-17</i> > pPD107.94/mk84-148
5'AACGATGGATACGCTAACAACTTGG3'	forward nested	<i>egl-17</i> > promoter	<i>egl-17</i> > pPD107.94/mk84-148
5'TTTCTGAGCTCGGTACCCTCCAAG3'	reverse	<i>egl-17</i> > promoter	<i>egl-17</i> > pPD107.94/mk84-148
5'TTAATATTTCTCTCTTGCAGGAACATG TCCTCGAATTTTCCCGAATTG3'	<i>unc-62</i> extension, forward	<i>RDE-1</i>	N2 gDNA
5'AAATTTCAAGTAATTTATGAAAACG3'	reverse	<i>RDE-1</i>	N2 gDNA
5'CAAGTAATTTATGAAAACGTTAG3'	reverse nested	<i>RDE-1</i>	N2 gDNA
5'CTTGAGGGTACCGAGCTCAGAAAAT GCGTTACGCTCTTGCCGCT3'	<i>egl-17</i> extension, forward	<i>HA-βtail</i>	<i>ost-1</i> > <i>HA-βtail</i>
5'TCACCTTCCACTGAGCCTCAAACC3'	reverse	<i>HA-βtail</i>	<i>ost-1</i> > <i>HA-βtail</i>
5'TTCCGATCTTTCTTGCATCGTGCTC3'	reverse nested	<i>HA-βtail</i>	<i>ost-1</i> > <i>HA-βtail</i>